



Edge U-Net: Brain tumor segmentation using MRI based on deep U-Net model with boundary information

Ahmed M. Gab Allah^{a,1,*}, Amany M. Sarhan^{b,2}, Nada M. Elshennawy^{b,3}

^a Department of Information Systems, Faculty of Computers and Artificial Intelligence, University of Sadat City, Sadat City, Egypt

^b Department of Computers and Control Engineering, Faculty of Engineering, Tanta University, Tanta, Egypt



ARTICLE INFO

Keywords:

Brain tumor segmentation
Boundary information
Convolutional neural network
MRI
Deep learning
Contrast limited adaptive histogram equalisation

ABSTRACT

Blood clots in the brain are frequently caused by brain tumors. Early detection of these clots has the potential to significantly lower morbidity and mortality in cases of brain cancer. It is thus indispensable for a proper brain tumor diagnosis and treatment that tumor tissue magnetic resonance images (MRI) be accurately segmented. Several deep learning approaches to the segmentation of brain tumor MRIs have been proposed, each having been designed to properly map out ‘boundaries’ and thus achieve highly accurate segmentation. This study introduces a deep convolution neural network (DCNN), named the Edge U-Net model, built as an encoder-decoder structure inspired by the U-Net architecture. The Edge U-Net model can more precisely localise tumors by merging boundary-related MRI data with the main data from brain MRIs. In the decoder phase, boundary-related information from original MRIs of different scales is integrated with the appropriate adjacent contextual information. A novel loss function was added to this segmentation model to improve performance. This loss function is enhanced with boundary information, allowing the learning process to produce more precise results. In the conducted experiments, a public dataset with 3064 T1-Weighted Contrast Enhancement (T1-CE) images of three well-known brain tumor types were used. The experiment demonstrated that the proposed framework achieved satisfactory Dice score values compared with state-of-art models, with highly accurate differentiation of brain tissues. It achieved Dice scores of 88.8 % for meningioma, 91.76 % for glioma, and 87.28 % for pituitary tumors. Computations of other performance metrics such as the Jaccard index, sensitivity, and specificity were also conducted. According to the results, the Edge U-Net model is a potential diagnostic tool that can be used to help radiologists more precisely segment brain tumor tissue images.

1. Introduction

A brain tumor is defined as a mass of tissues that grows gradually from abnormal cells. Whether or not they are malignant, brain tumors can harm nearby brain tissue through the added pressure they create within the rigid skull (Haj-Hosseini et al., 2016). Thus, early detection of brain tumors is essential for prompt and effective therapy (Anitha & Murugavalli, 2016). The human brain may be afflicted by multiple types of tumors, including gliomas, meningiomas, and pituitary tumors (Ricci & Dungan, 2001).

Computer-aided diagnostic (CAD) technologies were created and put

into use to assist neuro-oncologists in the process of quickly and accurately identifying brain tumors. MRIs represent an invaluable approach that provides detailed images of tissues and organs of the human body. MRIs remain the most accurate method of localising brain tumors and identifying their dimensions (Wulandari, Sigit, & Bachtiar, 2018). Accurately analysed multi-dimensional data from MRIs can help localise and monitor disease progression and guide treatment.

Machine learning has been used for disease detection, prediction, classification, and image segmentation in the context of healthcare images. Segmentation and classification of breast cancer (Debele, Amirian, Ibenthal, Palm, & Schwenker, 2017; Kebede et al., 2020; Yu, Zhou,

* Corresponding author.

E-mail addresses: ahmed.salem@fcai.usc.edu.eg (A. M. Gab Allah), amany.sarhan@f-eng.tanta.edu.eg (A. M. Sarhan), Nada.elshennawy@f-eng.tanta.edu.eg (N. M. Elshennawy).

¹ ORCID: 0000-0001-8998-8411.

² ORCID: 0000-0002-0151-9619.

³ ORCID: 0000-0002-8407-2719.

Table 1

A summary of previous models.

Ref.	Dataset	Architecture	Pre-processing	Post-processing	Evaluation metric
(Almahfud et al., 2018)	Radiopedia.org	K-Means + Fuzzy C-Means	–	Median filter Morphological Area Selection	Acc.: 91.94
(Abdel-Maksoud et al., 2015)	DICOM Brain Web BRATS 2012	K-Means + Fuzzy C-Means	Median filter Skull Removal	–	Prec.: 90.5 Recall: 100.0 Acc.: 90.5
(Kaur & Sharma, 2017)	BRATS	Self-adaptive K-means clustering algorithm	Median filter Histogram equalisation	Sobel edge detection Median filter	–
(Blessy & Sulochana, 2015)	BRATS 2012	Unsupervised optimal fuzzy clustering algorithm	Intensity standardisation Histogram based Normalisation	–	Sens.: 94.0
(Sheela & Suganthi, 2019)	Cheng et al. (Cheng et al., 2015)	Greedy snake model + fuzzy C-means optimisation	Median filtering	Chose high maximum perimeter region	Spec.: 96.0 DS: 78.0, 59.0, 49.0 * Sens.: 67.0, 51.0, 44.0 * Spec.: 87.0, 88.0, 87.0 *
(Kaya et al., 2017)	–	Fuzzy C-Means + K-Means algorithms	PCA algorithms	–	Euclidean distances: 1.8656 Reconstruction error: 1.1597
(Ma et al., 2018)	BRATS 2013 BRATS 2015 BRATS 2017	Random Forests + Active contour model	–	–	DS: 89.0, 80.0, 72.0 ** Spec.: 90.0, 80.0, 66.0 ** Sens.: 85.0, 80.0, 82.0 **
(Ayachi & Ben Amor, 2009)	DICOM Author dataset	Support Vector Machine (SVM)	Image registration Anisotropic diffusion filtering	–	Percentage of correct classification: 79.89 %. Match percentage: 81.79 %. Sens.: 99.29 Spec.: 99.72 Acc.: 99.72
(Krishnakumar & Manivannan, 2021)	–	Rough k means clustering algorithm for segmentation + multi kernel support vector machine algorithm	Manual correction Gabor wavelet transform	–	Sens.: 99.29 Spec.: 99.72 Acc.: 99.72
(Pereira et al., 2016)	BRATS 2013 BRATS 2015	CNN	N4ITK method (Tustison et al., 2010) Intensity normalisation method (Nyúl, Udupa, & Zhang, 2000)	Volumetric constrains used to remove clustering the smaller than threshold	DS: 88.0, 83.0, 77.0 ** Sens.: 89.0, 83.0, 81.0 ** PPV: 88.0, 87.0, 74.0 **
(Thaha et al., 2019)	BRATS 2015	Enhanced Convolutional Neural Networks + BAT algorithm loss function	Skull stripping Morphological operation (thicken) Normalisation	–	Prec.: 87.0 Recall: 90.0 Acc.: 92.0
(Havaei et al., 2017)	BRATS 2013	Introduced CNN architecture	Remove the highest and lowest 1 % intensities.	Remove flat blobs	DS: 84.0, 71.0, 57.0 ** Spec.: 88.0, 79.0, 54.0 ** Sens.: 84.0, 72.0, 68.0 **
(Sajid et al., 2019)	BRATS 2013	Hybrid Convolutional Neural Network	N4ITK Normalisation N4ITK Normalisation	Morphological operations (Erosion, Dilatation)	DS: 86.0, 86.0, 88.0 ** Sens.: 86.0, 87.0, 90.0 ** Spec.: 91.0, 93.0, 94.0 **
(Díaz-Pernas et al., 2021)	Cheng et al. (Cheng et al., 2015)	DCNN that includes a multiscale approach	Normalisation	–	DS: 89.4, 77.9, 81.3 * Sens.: 89.77, 91.47, 89.68. * Pttas: 93.8, 98.6, 97.9 *
(Sun et al., 2019)	MRBrainS13 MALC12	Spatially Weighted-3D network-UNet	–	–	DS: 86.6, 89.9, 84.8 *** Hausdorff distance: 1.29, 1.73, 1.84 *** Absolute volume difference: 5.75, 5.47, 6.84 ***
(Ding et al., 2019)	BRATS 2015	Stack Multi-Connection Simple Reducing Net	Normalisation	–	DS: 83.12, 67.1, 59.19 ** Prec.: 78.96 ** Sens.: 90.25 **
(Maji et al., 2022)	BRATS 2019	Attention Res-UNet with Guided Decoder	Normalisation	–	DS: 91.1, 87.6, 80.1 ** IOU: 83.8, 78.1, 66.0 **

DS: Dice score in (%), Sens.: Sensitivity (%), Spec.: Specificity (%), Acc.: Accuracy (%), PPV: positive predictive value, IOU: Intersection over Union (%), and Prec.: Precision (%).

* Where these values refer to meningioma, glioma, and pituitary tumor, respectively.

** Where these values refer to complete, core, and enhancing tumor, respectively.

*** White matter, gray matter, and cerebrospinal fluid.

Wang, & Zhang, 2022), brain tumors (Gab Allah, Sarhan, & Elshennawy, 2021; Megersa & Alemu, 2015), and such tumors as lung and colon cancers have received the bulk of recent related research (Debelee, Kebede, Schwenger, & Shewarega, 2020).

In the current clinical practice, the majority of brain tumor image analysis is performed manually. This is both time-consuming and prone to human error, especially if not performed by a disease expert (Işın, Direkoglu, & Şah, 2016). Segmentation of healthy and pathologic brain tissue in MRIs, including subregion determination, is critical for analysing brain tumors and selecting treatment plans, as well as for successful cancer research (Bauer, Nolte, & Reyes, 2011). Segmentation of brain tumor MRIs is significantly important for better tumor diagnosis and treatment, as reported in (Menze et al., 2014).

The brain tumor segmentation research field has grown significantly in recent years, with a plethora of segmentation methods proposed using various datasets. There are three types of recently developed segmentation models: clustering-based segmentation, supervised machine learning segmentation, and deep learning segmentation.

The clustering-based approaches to segmentation work through the partitioning of MRIs into several disjoint groups and identifying a region of interest (ROI) within each image. Pixels with high levels of similarity within each region are classified as such, whereas distinct pixels are classified as such. K-means clustering is an unsupervised machine learning-based algorithm commonly used to extract a ROI from other image elements. It has been investigated as a method of brain tumor segmentation, with acceptable accuracy despite requiring only minimal computational time and power (Almahfud, Setyawan, Sari, & Rachmawanto, 2018). K-means has been found to be most suitable for large datasets. Its drawbacks include insufficient delineation of the tumor region and sensitivity to outliers (Abdel-Maksoud, Elmogy, & Al-Awadi, 2015). To address these vulnerabilities, a more advanced self-adaptive K-means algorithm was created (Kaur & Sharma, 2017). Using the Fuzzy C-Means algorithm, things that are likely to belong to multiple classes are clustered according to their degree of 'belonging' to each class (FCM). Pixels can thus occupy multiple clusters. When it comes to noise-free image segmentation, FCM outperforms hard-clustering methods like K-means. The efficacy of FCMs decreases in brain tumors, where segmenting MRIs is susceptible to the effects of 'unknown noise' (Blessy & Sulochana, 2015). A method was proposed by (Sheela & Suganthi, 2019) to overcome the disadvantages of FCMs. For automatic learning, the researchers used the greedy snake algorithm in addition to FCM optimisation.

T1 weighted clustering is used to segment tumor tissues captured in brain MRIs using Principal Component Analysis (PCA) algorithms. In (Kaya, Pehlivanlı, Sekizkardeş, & İbrikci, 2017), a comparison between the tumor portion and remaining parts of each brain image was performed. The predicted tumor portion could not be clearly identified. Clustering may result in inaccurate detection of tumor size, possibly leading to incorrect treatment, increased morbidity and mortality.

Other models of brain tumor MRI segmentation have been based on supervised machine learning, in which the segmentation problem is converted to a tumor pixel classification problem, with the image extracted features serving as input to the model and the desired classes of segmentation serving as output. Supervised machine learning algorithms have been incorporated into a number of proposed segmentation processes of brain tumor images. In the study by (Ma, Luo, & Wang, 2018), automatic segmentation involved a combination of a random forest algorithm and an active contour model. A support vector machine was also used in a study by (Ayachi & Ben Amor, 2009). In that study model, a combination of the two-approaches employed Gabor wavelet transform (IGWT) as feature extractor and K-means for the purposes of clustering. Finally, to achieve the most accurate classification of brain tissue into tumor and non-tumor, a multi-kernel support vector machine (MK SVM) algorithm was then run (Krishnakumar & Manivannan, 2021).

In the deep learning methodologies, MRIs typically go through a

number of deep learning building blocks, and the features that are extracted determine how MRIs are segmented. In the segmentation of brain tumors, various deep learning models have been used. DCNNs have been enhanced with 3×3 filters to achieve automatic brain tumor segmentation (Pereira, Pinto, Alves, & Silva, 2016). To improve segmentation while reducing processing time, an Enhanced Convolutional Neural Network (ECNN) model with an optimised loss function was added. For binary segmentation, a BAT algorithm was developed (Thaha et al., 2019). To solve the problem of imbalanced tumor labels, a multi-layer CNN model with a two-pathway architecture was created. For each voxel, the segmentation task was treated as a multiple classification task (Havaei et al., 2017). Another Hybrid CNN model was created with a patch-based method. To address the issue of imbalanced data, the model was programmed to take into account both contextual and local data. This involved using a two-phase training procedure (Sajid, Hussain, & Sarwar, 2019). In contrast to previous models, the Multiscale-CNN (Díaz-Pernas et al., 2021) model was designed with three pathways to capture features at three spatial scales. Fully convolutional networks (FCNs) were developed to generate the label map for the entire image, overcoming the previous methods' two limitations of computational cost and patch size selection (Long, Shelhamer, & Darrell, 2015). (Ronneberger, Fischer, & Brox, 2015) proposed a U-Net inspired by (Long et al., 2015), which was built using a symmetric fully convolutional network. This model achieved high accuracy, particularly when applied to medical images. A 3D glioma segmentation method based on sequential U-Nets was later introduced (Sun et al., 2019), having a fully automated brain tumor segmentation network based on a stacked U-Net architecture (Ding et al., 2019). Another U-Net-based model is the Attention Res-UNet with Guided Decoder (ARU-GD), in which the learning process is optimised for each decoder block. Each decoder block was also designed to employ its own loss function (Maji, Sigedar, & Singh, 2022).

The following section details our proposed MRI brain tumor segmentation framework. Table 1 summarises prior brain tumor segmentation models.

Although many deep neural network-based models have achieved success, there are still many challenges and limitations found, including intensity variation of brain tumor tissues due to the imaging protocol being used, modality of images, and random noise inherent in MRI systems (Prima, Ayache, Barrick, & Roberts, 2001), which may result in vague tissue texture and a blurry boundaries of tumor tissue. Furthermore, multiple classes or tissues can coexist within a single pixel of a brain image, a phenomenon known as the partial volume effect in MRIs (Arabahmadi, Farahbakhsh, & Rezazadeh, 2022; Hesamian, Jia, He, & Kennedy, 2019). The rough boundary of a brain tumor is perceived as another type of issue by brain tumor segmentation models. Besides that, brain tumors can vary in location, size, and shape within the brain (Wang & Chung, 2022).

We developed a new framework for automated brain tumor segmentation to resolve some of these issues. Brain MRIs are manipulated in this framework to reduce background noise during the imaging process. The U-Net architecture (Ronneberger et al., 2015) inspired the development of a novel encoder-decoder CNN model. To achieve more accurate tumor tissue segmentation, this encoder-decoder model considers brain MRI boundaries and is guided by an edge guidance block (EGB) module. Finally, an efficient loss function aids in dealing with both tumor boundaries and tumor tissue at the same time. The model was tested against the public brain tumor segmentation datasets created by Cheng et al. (Cheng et al., 2015), which contain MRIs of three different types of brain tumors (meningiomas, gliomas, and pituitary tumors). The proposed framework was shown to outperform the state-of-art models of brain tumor segmentation.

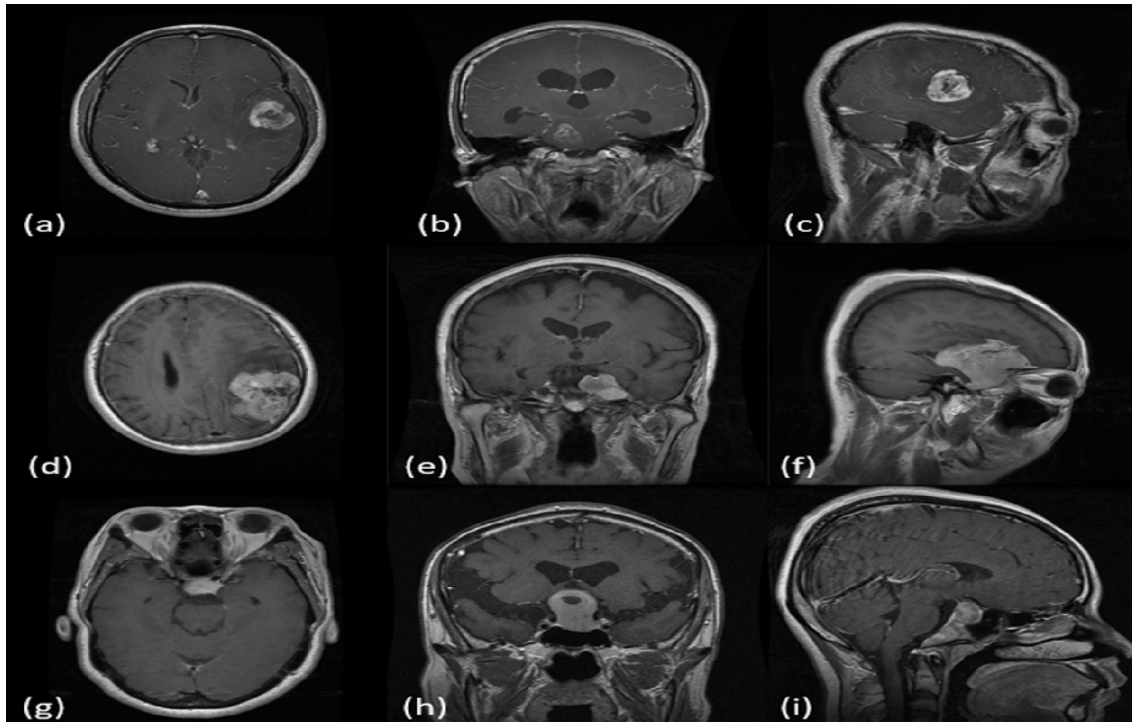
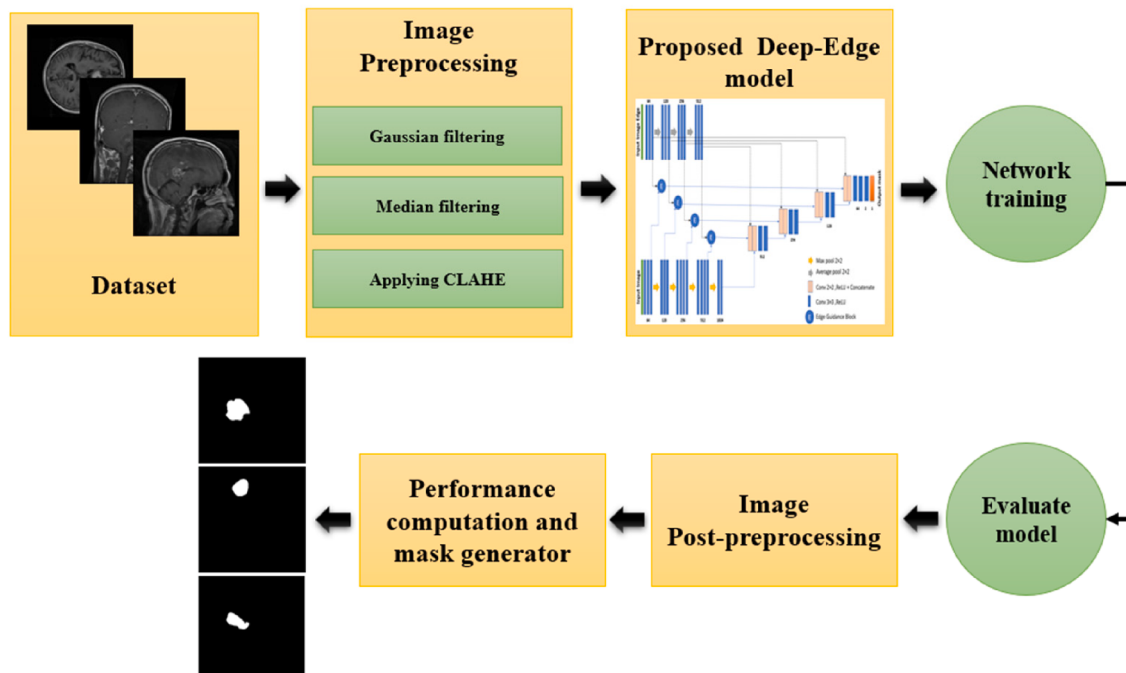
To address the aforementioned research issues and improve upon the performance of previous segmentation models, this work attempted to introduce the precise segmentation framework through the following contributions:

Table 2

Details of the (Cheng et al., 2015) MRI brain tumor dataset.

Type	No. brain tumor MRI
Meningioma	708
Gliomas	1426
Pituitary tumors	930
Total	3064

- Developing a U-Net structure-based deep-edge brain tumor MRI segmentation learning model, with a focus on MRI boundaries. Results showed that the framework's performance was able to outperform current state-of-the-art models.
- Suggesting the use of contrast limited adaptive histogram equalisation (CLAHE) in order to enhance MRI contrast and achieve better brain tumor segmentation.
- Designing an EGB module that fuses the original MRI boundary features with other MRI features. The outcomes of our framework

**Fig. 1.** Three samples for the three plans of brain MRI tumors from the dataset. (a, b, c) glioma, (d, e, f) meningioma, and (g, h, i) pituitary.**Fig. 2.** Block diagram for the proposed framework.

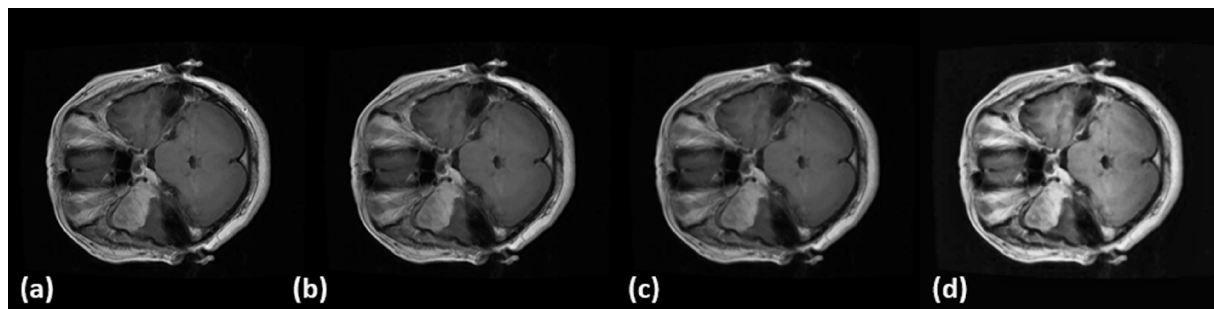


Fig. 3. Samples of brain tumor MRI and various filtering process: (a) original MRI, (b) After Gaussian filter, (c) After median filter, and (d) after CLAHE.

showed that the EGB had provided more boundary information, improving the ability to detect tumor location and shape recognition. • Developing a novel loss function for our edge deep learning model in which we combined pixel loss and boundary loss, allowing for better recognition of boundaries and, as a result, better pixel values, resulting in a better overall performance.

The remaining part of this paper is organised as follows: Section 2 describes how the used dataset was created and provides a detailed description of it. Section 3 provides a description of the proposed framework. Section 4 describes the results of the experiments and discusses the model's performance. Conclusions and suggestions for possible future work are presented in section 5.

2. Dataset for the study

The public dataset used in this study was created by Cheng et al. (Cheng et al., 2015) is the most commonly used brain tumor dataset and covers three types of brain tumors. It contains 3064 T1-CE MRIs of 233 patients with gliomas, meningiomas and pituitary tumors with a 512 × 512 pixel resolution. This dataset also includes tumor ground truths to help determine abnormal regions. Table 2 shows the distribution of the dataset's three types of tumors. Imagines of the three planes (axial, sagittal, and coronal) are available for the three types of tumors. Fig. 1 depicts a sample of each tumor type with different planes.

3. Methodology

This section presents the proposed segmentation framework in depth. Because of the high success of the U-Net model in medical image segmentation, we based our model on it. We designed an Edge U-Net model that uses the MRI and MRI boundaries as inputs. In addition, we enhanced the skip connection between opposite blocks in the U-Net model with EGBs to improve the ability of the framework to handle MRI boundaries at the decoder stage. Furthermore, a novel loss function was developed.

3.1. Architecture of proposed framework

Fig. 2 depicts the proposed segmentation framework. As shown in Fig. 2, the proposed framework has three major phases: pre-processing, Edge U-Net segmentation model, and post-processing. In the following subsections, we discuss the pre-processing techniques used on the MRI datasets, as well as the augmentation method used.

3.2. Image pre-processing phase

Image denoising is done during this stage. The main objective of MRI denoising is to obtain an improved image from a noisy MRI. Medical imaging is susceptible to noise from a variety of sources, including an electrical signal from a device or a camera sensor malfunction. Taking MRIs consumes both time and money. If noise is visible in the first

image, new images are rarely requested. The quality of an image has a significant impact on the subsequent segmentation process. Brain tumor segmentation is used to distinguish malignant tissue from other features of the brain, such as oedema and cerebrospinal fluid collections in addition to the normal brain tissue. MRIs need to be maintained at the edge of the image first. Filters and pre-processing techniques are used to address noise and other MRI flaws. They were designed to produce the clearest, most representative MRIs possible, allowing for the most accurate segmentation process.

To deal with MRI noise, we used multiple pre-processing steps in our framework. Gaussian and median filters were applied to the first step. Following that, we used CLAHE to improve the contrast of the MRI.

3.2.1. Gaussian filter

The use of size 5×5 Gaussian filters, as defined by Eq. (1), for edge detection during pre-processing would also assist in edge position displacement, edge vanishing, and phantom edges from MRI (Deng & Cahill, 1993).

$$G(x, y) = \frac{1}{2\pi\sigma^2} e^{-(x^2+y^2)/2\sigma^2} \quad (1)$$

where x and y represent size of kernel filter, and σ^2 is called the variance of Gaussian filter.

3.2.2. Median filter

The median filter (Sheela & Suganthi, 2019) is a second filter in our model. It is used for degraded image denoising and edge determination. This filter works by replacing each value with the median value of adjacent pixels (Gupta, 2011). A series of steps are required to calculate median filtering. First, the values of the target and neighbouring pixels are read. The pixel values are then arranged in ascending order. Finally, the value in the middle is chosen as the new pixel value (x, y). Eq. (2) shows how to calculate median filtering for input pixels (s, t).

$$F(x, y) = \text{median}_{(s,t) \in S_{xy}} \{g(s, t)\} \quad (2)$$

3.2.3. Image contrast enhancement

HE was used in this model to improve model performance by increasing the contrast of MRIs. Contrast is defined as the variation in object colour and/or brightness with respect to each other. Applications of contrast enhancement have traditionally included medical image processing, where its use in pre-processing has been shown to be both simple and effective (Kim, 1997).

In this work, we employed CLAHE, a variant of Adaptive Histogram Equalisation (AHE). CLAHE, unlike HE, divides an MRI into small rectangular shaped portions and applies its function to each portion individually. CLAHE has been used in numerous previous studies to improve local contrast and edge sharpness (Zuiderveld, 1994). It has also been demonstrated that limiting amplification improves the illumination of low-illumination images (Zuiderveld, 1994). In this study, contrast was increased by using CLAHE with a clipping factor of 2 and a kernel size of 8×8 . Fig. 3 depicts the results of applying various filters to an MRI.

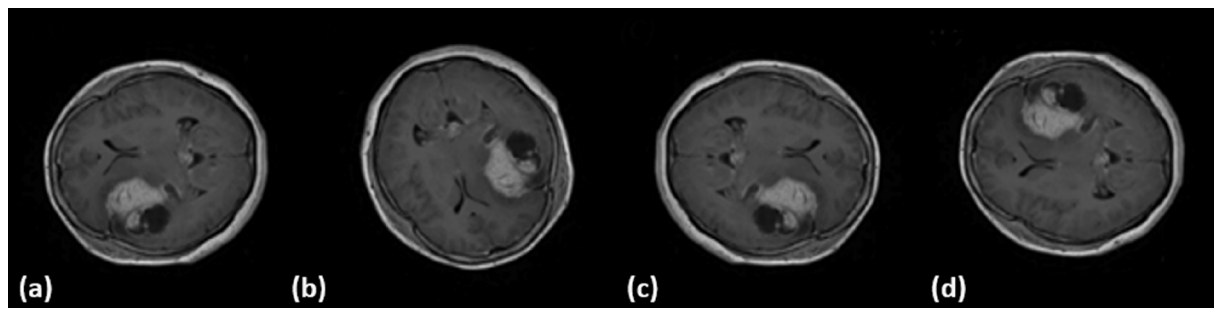


Fig. 4. Examples of the MRI augmentation process for brain tumors include (a) main MRI, (b) MRI rotation by 180 degrees, (c) MRI left mirroring, and (d) MRI up flipping.

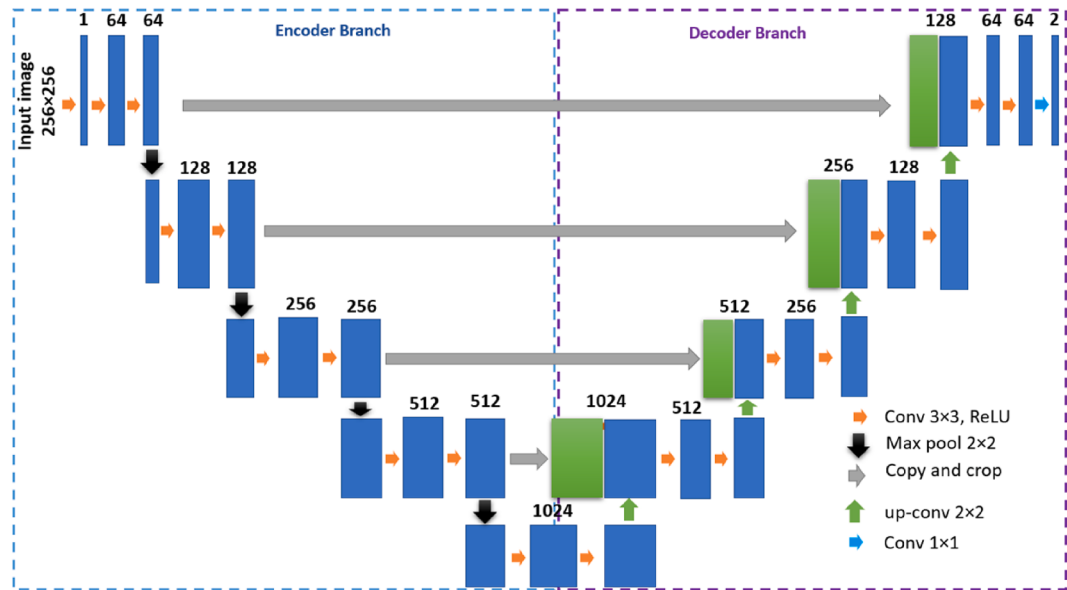


Fig. 5. Block diagram of U-Net model (Ronneberger et al., 2015).

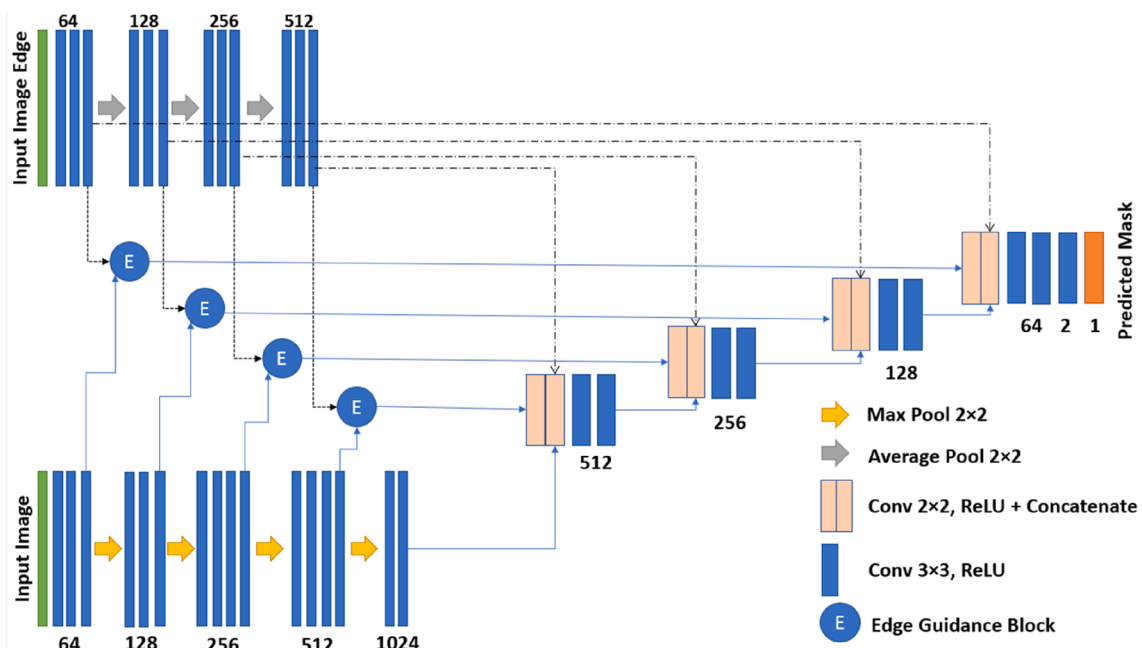


Fig. 6. Block diagram of the MRI brain tumor segmentation framework.

Fig. 3 shows that image quality had greatly improved, potentially allowing for better segmentation performance afterwards.

3.2.4. Data augmentation

An augmenter is used in this process to increase the size of the dataset in order to prevent overfitting. This augmentation is used on MRIs to change the position of the brain and prevent the model from memorising the location of tumors. Augmentation is accomplished through three operations: (a) MRI rotation at 90, 180, and 270 degrees without cropping; (b) right and left mirrored; and (c) flipping, in which the images are turned upside-down. Augmentation, like the samples in **Fig. 4**, increases the number of MRIs in all positions, including axial, sagittal, and coronal.

3.3. Proposed Edge U-Net network architecture

The most reliable method for radiologists to locate brain tumors is magnetic resonance imaging. The primary goal of this work was to introduce an intelligent system model that can more effectively segment the MRIs of three major brain tumors, namely gliomas, meningiomas, and pituitary tumors. A U-Net architecture was used to accomplish this goal. The basic U-Net architecture (Ronneberger et al., 2015), as shown in **Fig. 5**, consists of two branches: an encoder branch and a decoder branch. The structure of a U-Net encoder branch is similar to that of CNNs; convolutional operations are followed by down-sampling for feature extraction at the encoder levels. The second, decoding branch, consists of an up-sampling and concatenation layer followed by regular convolutional operations. Thus, the decoding branch semantically applies learnt discriminative features to the pixel space via the encoder network, achieving dense classification. A skip connection between the same-level layers of the encoder and decoder enables concatenating feature maps from the encoder network with the up-sampled feature map functioning to handover coarse global contextual information. During down-sampling, this method facilitates the recovery of local features.

Fig. 6 depicts the overall architecture of the proposed Edge U-Net model, with the U-Net serving as its backbone. The model takes two inputs: an image and its edges. The model's output is the mask of a brain tumor. In the proposed model, we used 256×256 input MRIs. These input MRIs are progressively filtered and down-sampled by a factor of two after each encoder block. Following this technique, the output size is reduced to 1/16 of the input MRI after the last encoder block, i.e., $1024 \times 16 \times 16$ is the dimension of feature maps after encoder blocks. The decoder part consists of four blocks that are coupled with the corresponding encoder blocks in the MRI as well as the MRI itself. The EGB is used for the detection and highlighting of boundary information. The EGB was added to address the degradation and saturation issues, improve extracted features at each block, and aid in the restoration of the input image. The fundamental decoder block is made up of two 3×3 convolutional layers with ReLU activation. In the model's final block, a sigmoid layer, and a convolutional layer with a 2×2 kernel size was added to forecast the picture mask. The feature maps are transformed to probabilities $\sigma(x)$ by sigmoid activation, as defined by Eq. (3) (Goodfellow, Bengio, & Courville, 2016).

$$\sigma(x) = \frac{1}{1 + e^{-x}} \quad (3)$$

where the x is the value of input pixel in n -dimensional matrix and $\sigma(x)$ is probability of each pixel belonging to the same class. As a result, the final output channels of the model become probability maps for masks. The loss function is calculated between the output and ground truth.

3.3.1. Image encoder branch

The image's encoder branch was modelled after VGG16 (Simonyan & Zisserman, 2014). The branch contains five convolutional blocks with

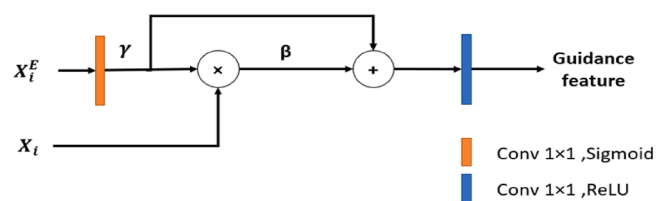


Fig. 7. Details and calculation flow of EGB.

256×256 input images. Each block is designed to extract features specific to a given input scale. The first block contains three convolution layers with 64 channels. The second block includes three convolution layers with 128 channels. The third block consists of four convolution layers with 256 channels each. The fourth block consists of four convolution layers with 512 channels. The final block includes two convolution layers with 1024 channels each, as well as a dropout layer with a factor of 0.5. All blocks have kernels of size 3×3 and ReLU activation functions with strides of 1, with the exception of the final block, which was designed with a kernel of size 1×1 . After each block, a Max Pooling layer was added, with kernels of size 2×2 and strides of 1.

3.3.2. Edge encoder branch

Four side outputs generate four features with different channel numbers for different scales of image edges. The input is a 256×256 pixel-edge image. In this case, we used a DCNN architecture to learn discriminant saliency features. Each edge encoder branch has four blocks with feature maps of 64, 128, 256, and 512. Each level is in charge of extracting the features unique to a given input scale. Each block includes three convolution layers with a kernel size of 1×1 and a ReLU activation function. Following each block, an average pooling layer with a kernel size of 2×2 and stride of 1 was added.

3.3.3. Edge guidance block (EGB)

Information loss is a problem for decoders. To concatenate encoder and decoder features, encoder-decoder networks designed for segmentation tasks always include skip connections (Badrinarayanan, Kendall, & SegNet, 2015; Simonyan & Zisserman, 2014). Brain tumors share characteristics, such as a similar 'background.' Their boundary information is frequently difficult to discern. As a result, various models with the ability to combine different brain tumor features have been developed (Alqazzaz, Sun, Yang, & Nokes, 2019; Maji et al., 2022).

We proposed using an EGB to direct the model's integration of picture boundary features into the various decoder blocks, mixing the features with various semantic data. This was inspired by the work of (X. Wang, Yu, Dong, & Loy, 2018). **Fig. 7** depicts the architecture of the EGB module.

To merge the edge feature X_i^E with the feature X_i , we used an edge guidance block. EGB has two inputs: the first input is the edge feature X_i^E extracted feature from the image, and the second is the image itself X_i , which reuses deep spatial features, transforming them in order to recover the realistic texture of images. EGB is composed of two convolution layers. The first convolution layer works with the edge map, having a kernel size of 3×3 and a sigmoid activation layer and a stride of 1. The second layer has a kernel of size 3×3 and a ReLU activation layer and stride of 1. To pass edge features to the next layer of the network and take the guidance role, we aggregated the EGB into hierarchical feature maps. Eqs. (4) and (5) define the implementation of EGB with its two separate branches that produce two attributes (γ, β), based on the conditional features. (γ, β) are utilized to convert X_i into an edge-aware feature X_i^F :

$$\beta = X_i \odot \gamma \quad (4)$$

$$EGB(X_i^F | \gamma, \beta) = \delta(\beta + \gamma) \quad (5)$$

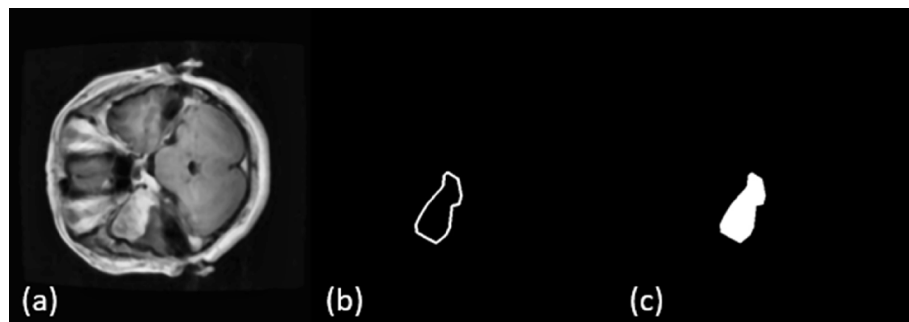


Fig. 8. Illustration of (a) MRI, (b) the mask edge generated from the ground truth, and (c) which are further region mask for brain tumor.

An element-wise operations were incorporated, with \odot as the production operation, $+$ as addition operation, and ∂ as the convolutional operation, with a kernel of size 3×3 and an ReLU activation function. EGB performs both feature-wise manipulation and spatial-wise transformation.

3.4. Loss function

Image segmentation and saliency detection are typically formulated as a problem of optimisation of a non-convex energy function with two terms: a data term and a regularisation term. The Mumford-Shah (MS) model (Mumford & Shah, 1989) is a mathematical global model whose goal is to convert the image segmentation task into an energy function minimisation task. The main goal of developing the most appropriate energy function for object segmentation is to reduce the value of the energy function to the lowest level required to achieve accurate segmentation. (Luo et al., 2017) developed a loss function that is the sum of cross entropy loss and boundary loss. Its goal was to minimise the Intersection-Over-Union (IOU) loss by increasing the symmetry rate between an image's predicted and real boundaries:

$$\text{Loss Function} \cong \underbrace{\sum_j \int S_j(y(v), \hat{y}(v)) dv}_{\text{Cross entropy loss}} + \underbrace{\sum_j (1 - \text{IOU}(S_j, \hat{S}_j))}_{\text{Boundary loss}} \quad (6)$$

where v is the pixel location, indexed by j , S_j is the total loss between ground truth (y) and predicted (\hat{y}) saliency map, $\text{IOU}(S_j, \hat{S}_j)$ is the IOU between the true boundary and the estimated boundary.

Fig. 8 illustrates the two terms and their impact on the robustness of a segmentation process. Fig. 8 depicts the tumor's boundary region (b). As shown in Fig. 8, the boundary loss function focuses on the mask edge, while the cross-entropy loss term focuses on the remaining regions to determine whether or not those regions represent tumor tissue (c). In the following subsections, we detail the relevant mathematical equations and their relationships with the aforementioned terms.

3.4.1. Cross entropy loss

The entropy loss function is widely used in medical image segmentation, and it has been shown to be effective in brain tumor segmenta-

tion (Jadon, 2020; Milletari, Navab, & Ahmadi, 2016). The cross-entropy function supports the completion of a segmentation task by retaining the global optimisation of an entire image. The cross-entropy loss function, as define in Eq. (7), has the advantage of focusing on the classification and regression of each pixel in the MRI. Focusing on global regions, it functions to minimise prediction errors with respect to the ground truth. The mathematical formulation of the cross-entirety loss function is as follows (Jadon, 2020):

$$\text{Cross Entropy Loss} = -(y \log(\hat{y}) + (1-y) \log(1-\hat{y})) \quad (7)$$

where \hat{y} is the predicted value by prediction model. In this work, the segmentation task is converted to a pixel level classification task guided by image boundaries, and the cross-entropy loss function is used to determine each masked pixel prediction error (regarding its corresponding ground truth). As such, the cross-entropy loss function is the first term of the main loss function in Eq. (6).

3.4.2. Boundary loss

Boundary loss can find its roots in significant dice loss function in medical image segmentation (Li, Li, & Wang, 2019; Milletari et al., 2016). To calculate the boundary loss, we sacrificed the saliency map gradient magnitude, using a Sobel operator with 3×3 filters, followed by a tanh activation (see Eq. (8)). Sobel operators can effectively distinguish boundaries of images by following Eq. (9) (Irwin, 1968):

$$G_x = \begin{bmatrix} -1 & 0 & 1 \\ -2 & 0 & 2 \\ -1 & 0 & 1 \end{bmatrix} \quad G_y = \begin{bmatrix} 1 & 2 & 1 \\ 0 & 0 & 0 \\ -1 & -2 & -1 \end{bmatrix} \quad (8)$$

$$G = \sqrt{G_x^2 + G_y^2} \quad \theta = \tanh G_y / G_x \quad (9)$$

The Sobel operator is used to separately calculate the difference between the values of boundary and non-boundary areas in order to run the learning phase with special attention to the boundary area. Weights are added to the lost values of the boundary areas for a more accurate learning phase. Given the gradient magnitude of saliency maps \hat{S}_j and gradient magnitude of true saliency maps S of region j , the boundary loss function is calculated using Eq. (10) (Tu, Ma, Li, Tang, & Luo, 2020).

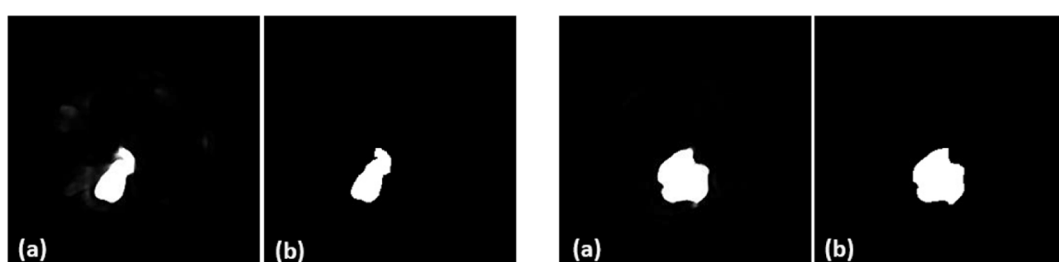


Fig. 9. Two samples showing post processing effect: (a) predicted mask, and (b) image after mask post-processing.

$$\text{Boundary loss} = 1 - \frac{2|S \cap \hat{S}_j|}{|S| + |\hat{S}_j|} \quad (10)$$

where the intersection operation is implemented by a point-wise multiplication operator.

3.5. Image post-processing

A morphological transformation and a simple thresholding technique are used in the final stage of the proposed framework. Based on the form of the input picture, a morphological gradient helps to reduce noise. Its action represents the differential between image dilation and erosion. The simple thresholding technique, defined as: $f(x, y) > t$, where t is a threshold value, is used to classify the pixel as either a predicted mask or a background pixel.

These techniques are used to remove small false positive values and blobs around the edges in order to produce a final predicted output (Biratu, Schwenker, Ayano, & Debelee, 2021; Magadza & Viriri, 2021) as a final step in which predicted masks are further processed (see Fig. 9). Tumor tissue images are clearly focused and defined after post-processing, as demonstrated.

4. Experimental results

A number of metrics were used to assess the performance and effectiveness of our proposed Edge U-Net brain tumor segmentation framework. The framework was trained and tested on the Cheng et al. dataset also different datasets were tested. During experimentation, two major questions were investigated. The first compared the proposed Edge U-Net brain tumor segmentation framework and pre-processing operations to the commonly used state-of-the-art models. The second assessed the proposed EGB module and loss function in order to confirm their superiority in producing more accurate segmentation results.

4.1. Implementation details

The proposed Edge U-Net model was built with a TensorFlow and Keras backend, and all experiments were run on Google Colaboratory environment servers with the NVIDIA Tesla P100 -PCIE GPU and 32.0 GB RAM. Adam optimiser (Frid-Adar et al., 2018) was chosen for the purposes of the learning process (being the most powerful optimiser). The initial learning rate was set at 0.0001, $\beta_1 = 0.9$, $\beta_2 = 0.999$, and $\epsilon = 1e-08$, with the learning rate decaying by 0.1 as it approached a plateau. The proposed model parameters were updated in an 8 mini batch. The maximum number of training epochs was set to 150. Normalisation was performed to avoid any complexity in the intensity values of image pixels. The pixel scale value was adjusted from (0–255) to (0–1) to minimise the complexity of the images by dividing image pixel values by 255, in addition to resizing the images. To reduce the complexity of model training, we resized the dataset MRIs to 256×256 pixels in size. We randomly split the dataset at nearly 90 % as a training group and other 10 % as a test group.

4.2. Evaluation metrics

The framework's effectiveness was evaluated using ten metrics that are commonly used to assess segmentation tasks. This study's dataset defines the ground truth for the abnormal regions used in evaluation metrics. The Dice score (Dice) and the Jaccard index (Jac) are the most important segmentation metrics. They are defined as:

$$\text{Dice} = \frac{2^*Tp}{2^*Tp + Fp + Fn} \quad (11)$$

$$\text{Jac} = \frac{Tp}{Tp + Fp + Fn} \quad (12)$$

Table 3

Comparison of Dice and Jac between proposed and state-of-arts methods on Cheng et al. dataset.

Methods	Metrics					
	Dice (%)			Jac (%)		
	Men.	Gli.	Pit.	Men.	Gli.	Pit.
FCN8 (Long et al., 2015)	78.63	86.32	85.20	64.79	75.93	74.21
U-Net (Ronneberger et al., 2015)	85.19	85.92	85.20	74.19	75.32	74.22
Res-UNet (Z. Zhang et al., 2018)	86.27	89.16	87.15	75.86	80.45	77.23
DeepLab V3+ (Chen et al., 2018)	83.60	88.5	86.25	71.83	79.37	75.82
Sheela et al. (Sheela & Suganthi, 2019)	78.0	59.0	49.0	—	—	—
Multiscale-CNN (Díaz-Pernas et al., 2021)	89.4	77.90	81.30	—	—	—
Sobhaninia et al. (Sobhaninia et al., 2020)	80.03*	—	—	—	—	—
El-Shafai et al. (El-Shafai et al., 2022)	35.18*	21.34*	—	—	—	—
Proposed Edge U-Net	88.8	91.76	87.28	79.85	84.78	77.43

* The authors introduce the result for MRI without classify it.

Additionally, pixel-wise specificity, sensitivity, and accuracy metrics are employed (Biratu et al., 2021). They are also defined as:

$$\text{Sensitivity} = \frac{Tp}{Tp + Fn} \quad (13)$$

$$\text{Specificity} = \frac{Tn}{Tn + Fp} \quad (14)$$

$$\text{Accuracy} = \frac{Tp + Tn}{Tp + Tn + Fn + Fp} \quad (15)$$

Finally, Precision, Area under the curve (AUC), Cohen's Kappa (Kappa), Matthew's correlation coefficient, and Average Hausdorff Distance (AHD) where A and B stand for the ground truth and predicted label, respectively (Al-Hadeethi, Abdulla, Diykh, & Green, 2021; Arab et al., 2020; Müller et al., 2022), defined as the formulas listed below:

$$\text{Precision} = \frac{Tp}{Tp + Fp} \quad (16)$$

$$\text{AUC} = 1 - 0.5 \left(\frac{Fp}{Tp + Fn} + \frac{Fn}{Tn + Fp} \right) \quad (17)$$

$$\text{Kappa} = \frac{(Tn + Fn)(Tn + Fp) + (Fp + Tp)(Fn + Tp)}{Tp + Tn + Fn + Fp} \quad (18)$$

$$\text{MCC} = \frac{(Tp * Tn) - (Fp * Fn)}{\sqrt{(Tp + Fp)(Tp + Fn)(Tn + Fp)(Tn + Fn)}} \quad (19)$$

$$\text{AHD} = \frac{1}{N} \sum_{a \in A} \min_{b \in B} \|a - b\| \quad (20)$$

where the four primary keys are number of: true positive (Tp), true negative (Tn), false positive (Fp), and false negative (Fn) values. The number of samples where both the proposed Edge U-Net model predicted label and the ground truth label promise the existence of tumor represented by Tp ; Tn represents the number of samples where both the proposed Edge U-Net model predicted label decision and the ground truth label assure the absence of tumor. Fn and Fp represent the number of samples where the decisions differ. Of all segmentation metrics, the Jac and Dice metrics are the most significant.

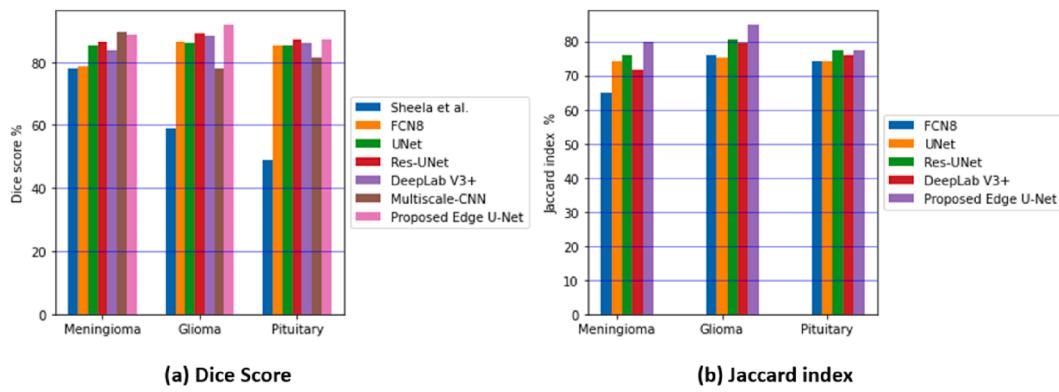


Fig. 10. Dice and Jac index for compared models ((Sheela & Suganthi, 2019), FCN8, U-Net, Res-UNet, DeepLab V3+, Multiscale-CNN (Díaz-Pernas et al., 2021), and Proposed Edge U-Net model).

4.3. Comparison to state-of-the-art methods

In this section, we detail a comparison of the proposed Edge U-Net model to a number of state-of-the-art methods on the same Cheng et al. dataset (Cheng et al., 2015). Then, to evaluate the robustness of our model performance, the proposed model (Edge U-Net) is compared against other models on different datasets.

4.3.1. Experimental results on (Cheng et al., 2015) dataset

Table 3 presents the performance results (in terms of Dice, Jac) of the proposed model against a number of state-of-the-art models: FCN8 (Chen, Zhu, Papandreou, Schroff, & Adam, 2018; Díaz-Pernas et al., 2021; El-Shafai et al., 2022; Long et al., 2015; Ronneberger et al., 2015; Sheela & Suganthi, 2019; Sobhaninia, Rezaei, Karimi, Emami, & Samavi, 2020; Z. Zhang, Liu, & Wang, 2018). As shown in table, the Edge U-Net model produced the best values for Dice, indicating that the Edge U-Net model has a high ability to generate a predicted mask for tumor tissue that is identical to the ground truth mask.

Many deep learning segmentation studies, such as (Chen et al., 2018; Díaz-Pernas et al., 2021; Long et al., 2015; Ronneberger et al., 2015; Sobhaninia et al., 2020; Zhang et al., 2018), which offered many deep learning models used for automatic segmentation of brain tumour types, are mentioned to further the significance of the Edge U-Net technique. For example, MRI segmentation using the FCN8 (Long et al., 2015) model significantly improves the segmentation by fusing several layer representations where pooling operators are swapped out for up-sampling operators. To achieve performance better than that of the FCN8 (Long et al., 2015) model, the study of the U-Net (Ronneberger et al., 2015) employs the skip connection after each block feature to transfer the features from the encoder to the decoder. Another encoder-decoder approach is DeepLab V3+ (Chen et al., 2018), which after encoding the rich contextual information utilizes a simple yet effective decoder module to extract object boundaries. While the Res-UNet

(Zhang et al., 2018) combines the benefits of residual learning with U-Net (Ronneberger et al., 2015). Both the skip connections inside the residual units and between the network's encoding and decoding channels will aid in the forward and backward computation of information.

The Edge U-Net model metrics, Dice and Jac values, indicated that our proposed model had outperformed all the state-of-the-art models with the three types of tumors. For meningiomas, the Dice stood at 88.8 % and the Jac at 79.85 %. These values indicated better performance compared with the other models, where Dice and Jac indices stood at 5.2 % and 8.02 % for DeepLab v3+; 2.53 % and 3.99 % for Res-UNet; 3.61 % and 5.66 % for U-Net; 10.17 % and 15.06 % for FCN8. Conversely, the Multiscale-CNN model (Díaz-Pernas et al., 2021) that uses a multi-pathway CNN model had the only Dice higher than our proposed model, with a difference of only 0.6 %. With gliomas, the proposed Edge U-Net model yielded the highest performance, with differences in Dice and Jac indices of 2.6 % and 4.33 % compared with the Res-UNet model, which stood in second place. Similarly, our model yielded the highest Dice (87.28 %) and Jac (77.43 %) with pituitary tumors. The network developed by Sobhaninia et al. (Sobhaninia et al., 2020) can be improved by using a cascade method with various MRI scales to achieve a Dice of 80.03 %. But it is clear that our suggested segmentation model worked better than their model.

The studies that use clustering for segmentation, like (Sheela & Suganthi, 2019), include a greedy snake approach in addition to FCM optimisation, resulting in the lowest Dice (78.0 %), sensitivity (67.0 %), and specificity (88.0 %) for meningiomas. Additionally, (El-Shafai et al., 2022) used particle swarm optimisation (PSO) and fast fuzzy C-means clustering (IFFCM) algorithms to detect meningiomas, gliomas, and pituitary tumors with Dice, Jac, sensitivity, specificity, and accuracy rates of 35.18 %, 21.34 %, 37.92 %, 96.19 %, and 93.47 %, respectively. Thus, compared to this research, other segmentation research reported, lower performance metric values.

Table 4

Comparison of sensitivity, specificity, accuracy, and precision between proposed model and state-of-arts methods on Cheng et al. dataset.

Methods	Metrics											
	Sensitivity (%)			Specificity (%)			Accuracy (%)			Precision (%)		
	Men.	Gli.	Pit.	Men.	Gli.	Pit.	Men.	Gli.	Pit.	Men.	Gli.	Pit.
FCN8 (Long et al., 2015)	74.26	91.24	80.2	99.62	99.11	99.75	99.0	98.77	99.21	74.26	91.24	80.68
U-Net (Ronneberger et al., 2015)	85.94	91.88	89.42	99.65	99.05	99.52	99.35	98.74	99.3	85.94	91.88	89.42
Res-UNet (Z. Zhang et al., 2018)	90.14	90.97	86.92	99.61	99.38	99.68	99.42	98.88	99.35	90.13	90.97	86.92
DeepLab V3+ (Chen et al., 2018)	89.77	91.47	89.68	99.51	99.29	99.57	99.32	98.95	99.34	89.77	91.46	91.68
Sheela et al. (Sheela & Suganthi, 2019)	67.0	51.0	44.0	87.0	88.0	87.0	—	—	—	—	—	—
Multiscale-CNN (Díaz-Pernas et al., 2021)	96.1	90.7	95.4	—	—	—	—	—	—	—	—	—
El-Shafai et al. (El-Shafai et al., 2022)	37.92*	96.19*	93.47*	32.81*	—	—	—	—	—	—	—	—
Proposed Edge U-Net	94.02	93.59	85.99	99.45	99.71	99.51	99.23	99.35	99.4	93.59	85.99	—

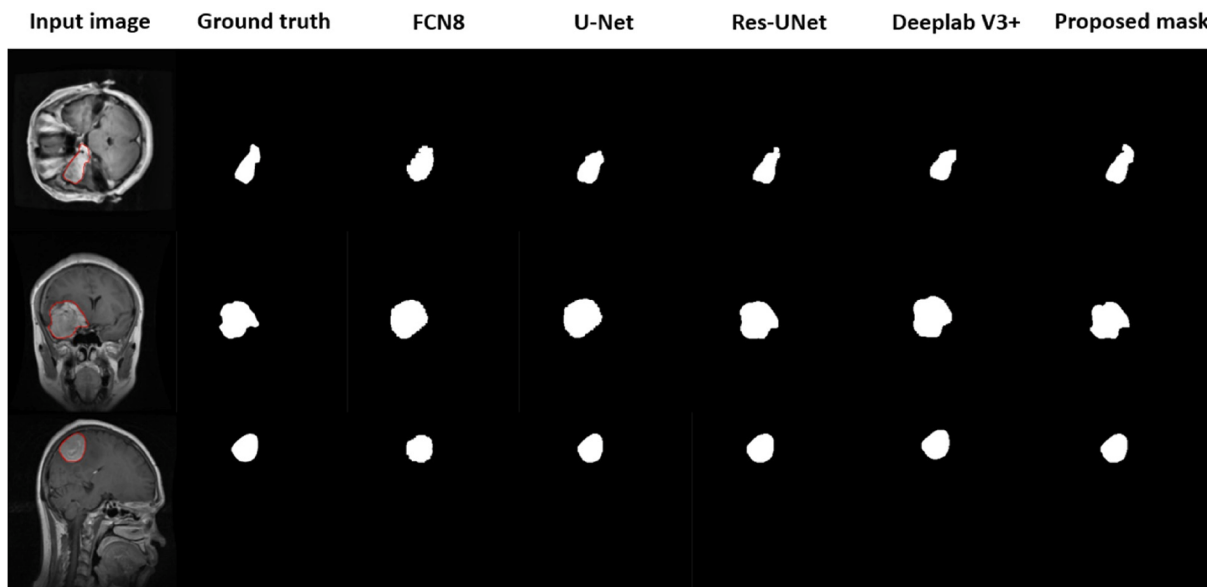
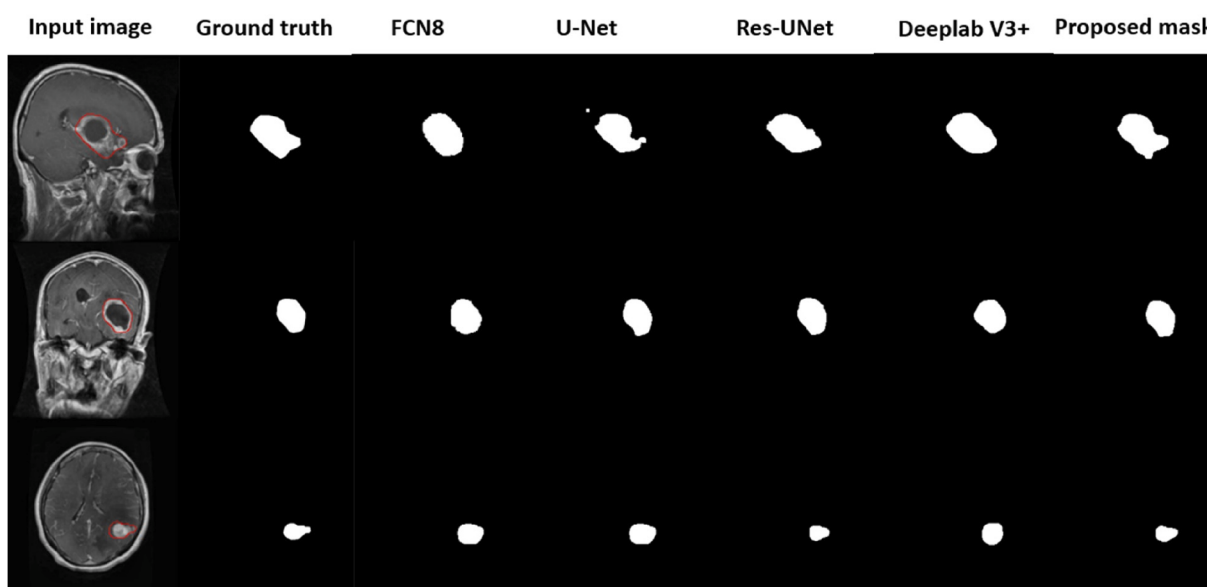
* The authors introduce the result for MRI without classify it.

Table 5

Comparison of MCC, AUC, Kappa, and AHD between proposed and state-of-arts methods on Cheng et al. dataset.

Methods	Metrics											
	MCC (%)			AUC (%)			Kappa (%)			AHD		
	Men.	Gli.	Pit.	Men.	Gli.	Pit.	Men.	Gli.	Pit.	Men.	Gli.	Pit.
FCN8 (Long et al., 2015)	78.26	85.81	84.94	91.45	90.76	94.85	78.12	85.68	84.79	10.63	16.12	8.25
U-Net (Ronneberger et al., 2015)	84.86	85.47	84.94	92.07	90.16	90.56	84.85	85.27	84.82	8.06	21.93	7.62
Res-UNet (Z. Zhang et al., 2018)	86.06	88.66	86.82	91.26	93.49	93.53	85.97	88.64	86.82	8.06	9.0	8.0
DeepLab V3+ (Chen et al., 2018)	83.47	87.99	82.24	89.0	92.66	87.15	83.26	87.94	81.78	16.03	8.94	8.06
(El-Shafai et al., 2022)	31.85*	—	—	—	—	—	—	—	—	—	—	—
Proposed Edge U-Net	85.99	91.38	86.96	93.91	94.85	94.12	88.5	91.36	86.95	8.0	7.62	7.07

* The authors in (El-Shafai et al., 2022) introduced the result for MRI without classifying it.

**Fig. 11.** Samples of meningiomas tumor MRI segmentation for FCN8, U-Net, Res-UNet, DeepLab V3+, and proposed Edge U-Net model for three planes (Red contour is the ground truth label).**Fig. 12.** Samples of glioma tumor MRI segmentation for FCN8, U-Net, Res-UNet, DeepLab V3+, and proposed Edge U-Net model for three planes (Red contour is the ground truth label).

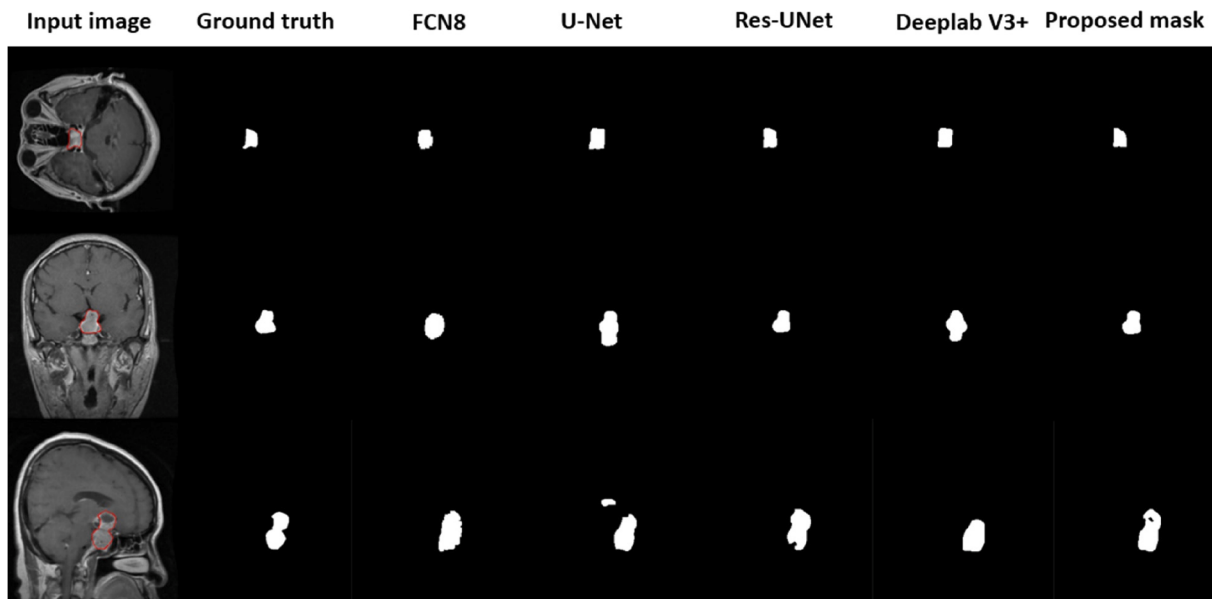


Fig. 13. Samples of pituitary tumor MRI segmentation for FCN8, U-Net, Res-UNet, DeepLab V3+, and proposed Edge U-Net model for three planes (Red contour is the ground truth).

Evidently, our model had generally outperformed the other models with respect to the three types of tumors. Thus, the proposed framework was shown to be best able to distinguish tumor tissue from other brain tissue (both normal and pathological), whilst most precisely following tumor tissue boundaries. Fig. 10 compares Dice and Jac scores of state-of-the-art models.

In addition to Dice and Jac metrics, Table 4 compares our model's sensitivity, specificity, accuracy, and precision to state-of-the-art models. Sensitivity describes how well the method detects tumors in MRI pixels. Specificity reports the ability to identify MRI pixels that do not have tumors. The suggested Edge U-Net model had sensitivity values of 94.02 percent, 93.59 percent, and 85.99 percent for meningiomas, gliomas, and pituitary tumors, respectively. This demonstrates that the Deep-Edge U-Net had accurately detected tumor-related pixels in MRIs. Similarly, the Edge U-Net model had specificities of 99.45 %, 99.5 %, and 99.71 % for meningiomas, gliomas, and pituitary tumors, respectively, indicating a strong ability to differentiate between tumor and non-tumor pixels. The Multiscale-CNN (Díaz-Pernas et al., 2021) model showed slightly better sensitivity results for meningiomas, whereas U-Net showed higher specificity for meningiomas. Edge U-Net has the highest precision value for glioma and has an acceptable value compared to other models, whereas Res-UNet and DeepLab V3+ have the highest for meningioma and pituitary tumor respectively. Finally,

accuracy indicates how a model classified every pixel class (tumor /non-tumor class). In comparison to the state-of-the-art models, our Edge U-Net model had the highest capacity to identify the pixels, with accuracy values for meningiomas, gliomas, and pituitary tumors of 99.51 %, 99.23 %, and 99.35 %, respectively.

Table 5 displays the outcomes for other performance metrics (MCC, AUC, Kappa, and AHD). The prediction mask produced good outcomes for all T_p , T_n , F_p , and F_n pixel values since the MCC for the Edge U-Net model had higher score values than other state-of-the-art models that were based on deep learning, except for the Res-UNet (Zhang et al., 2018) model with only 0.07 % higher in glioma tumor, and clustering-based segmentation. AUC is a measurement of a classifier's ability to distinguish between pixel classes (tumor/non-tumor class). The Edge U-Net model performs the best at differentiating between tumor and non-tumor pixels for meningioma and glioma, while FCN8 (Long et al., 2015) has the highest for pituitary with 0.73 % compared to the Edge U-Net model. All state-of-the-art proposed brain tumor segmentation models obtain a high Kappa metric value, meaning they have a remarkable capacity to manage challenges with unbalanced classes, but our model has the highest value, and it is evident that our model outperformed their models. In medical image segmentation, AHD is a commonly used performance metric used to calculate the distance between two images. It is used to measure the gap between the ground truth and predicted

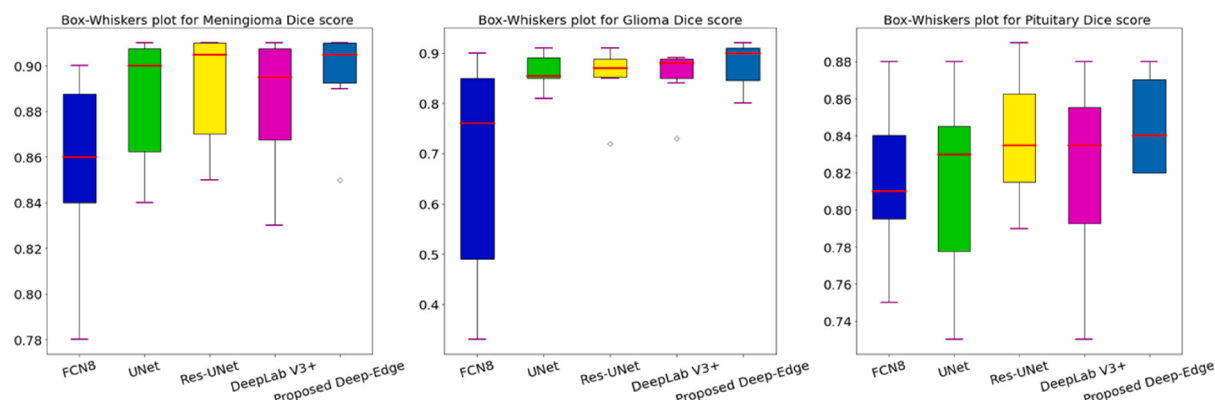


Fig. 14. Box-Whisker's plot for models Dice.

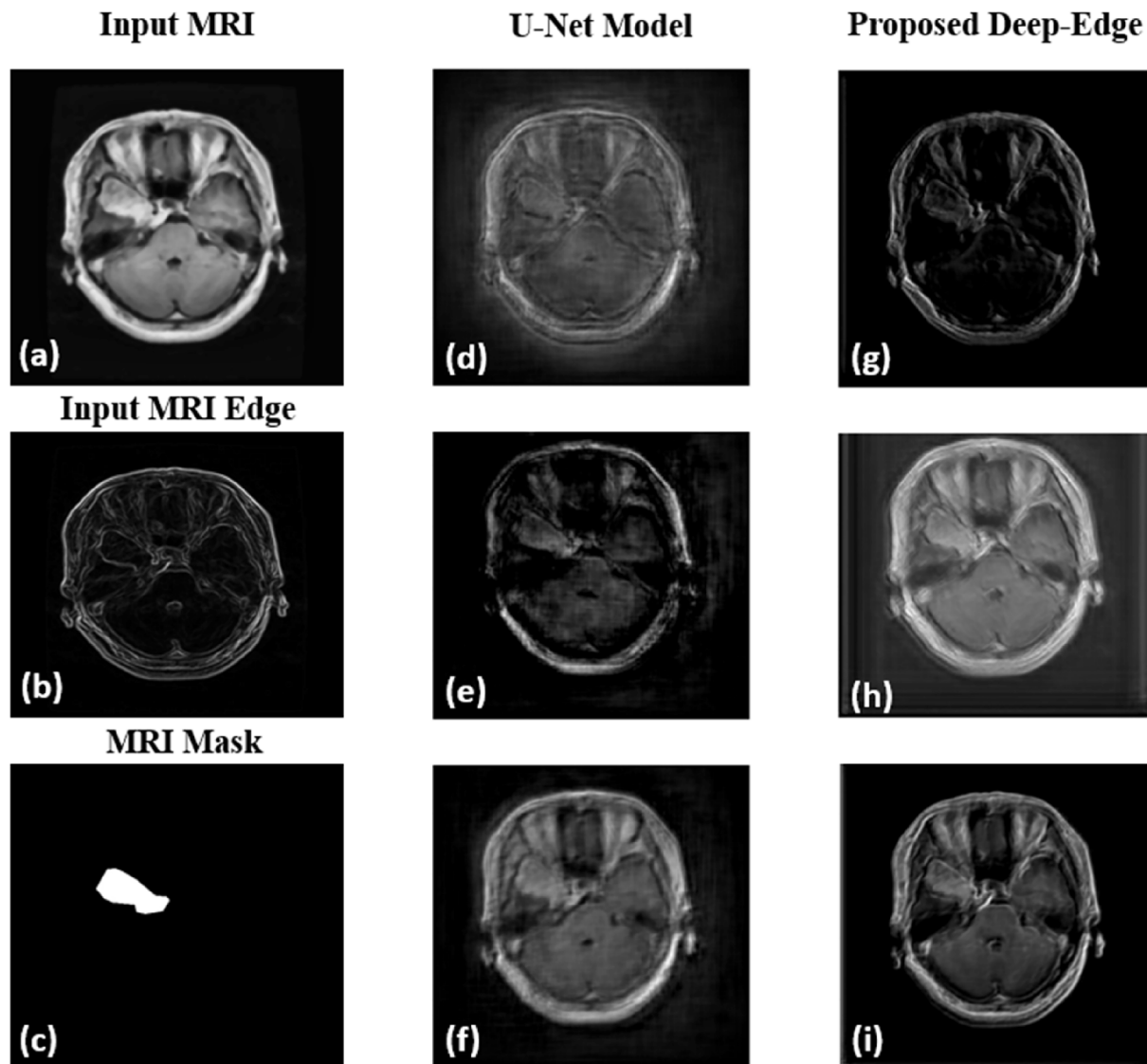


Fig. 15. Random selected feature maps of U-Net model and Proposed Edge U-Net for the same decoder block. (a) input MRI, (b) input MRI edge, (c), MRI mask, (d, e, f) feature maps of U-Net model, and (g, h, i) feature maps of proposed Edge U-Net model.

mask. Our proposed model achieves the shortest distance compared to other state-of-the-art models.

We also conducted a visual comparison of label maps of brain tumor tissues generated by the various models compared to the ground truth; shown in Figs. 11–13. The proposed model was able to produce label maps for meningiomas, gliomas, and pituitary tumors, guided by boundaries and focusing on tumor tissues, with little acquisition of other brain tissues, as shown in the figures. The other segmentation models produced varied results in terms of their ability to predict tumor tissues. These models, ordered from least to most efficacious, were: FCN8, UNet, Res-UNet, and DeepLab V3 +.

Fig. 14 shows a Box-Whisker plot of Dice of the proposed Edge U-Net model and the other state-of-art models. The plot illustrates the distribution of output Dice for each model. As the plots shows, the median values of Dice for proposed method were of higher values than the other methods (except for the Res-UNet, whose medians were equal to those of the proposed model for only meningioma).

As our DCNN was inspired by U-Net architecture, we compared the features maps generated from the last block for both proposed model and the U-Net model. As illustrated in Fig. 15, using EGB in the proposed Edge U-Net model facilitated the generation of feature maps which were advantageously supported with MRI boundaries, yielding better

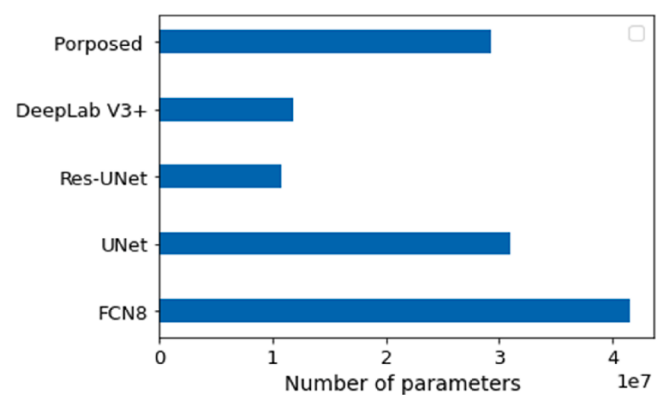


Fig. 16. The comparison of each state-of-the-art model's parameter numbers.

detection of tumor-affected tissues.

Our model also had the advantage of employing the most suitable loss functions; the binary cross-entropy loss function and the boundary loss function. With each type of loss function 'focusing' on its target, a

Table 6

Comparison of Dice and Jac for LGG and HGG between proposed and state-of-arts methods on different datasets.

Method	Dataset	Dice (%)		Jac (%)		Sensitivity (%)	
		LGG	HGG	LGG	HGG	LGG	HGG
(Kermi et al., 2018)	BRATS 2018	88.09	72.67	67.54	78.85	—	88.71
(Shehab et al., 2021)	BRATS 2015	79.04	89.87	68.18	82.1	94.41	93.47
(Russo et al., 2022)	BRATS 2016	88.4	90.7	—	—	—	—
BRATS 2017							
(Soleymanifard & Hamghalam, 2022)	BRATS 2017	85.0	90.0	—	—	—	—
(Huang & Wan, 2022)	BRATS 2018	78.13	90.10	66.95	82.12	—	90.48
Proposed Edge U-Net	Cheng et al. (Cheng et al., 2015)	Men.: 88.8 Pit.: 87.28	Gli.: 91.76 Pit.: 77.43	Men.: 79.85 Pit.: 84.78	Gli.: 84.78 Pit.: 77.43	Men.: 94.02 Gli.: 93.59 Pit.: 85.99	

Table 7

Comparison of Dice between proposed and state-of-arts methods on different datasets.

Methods	Dataset	Dice (%)	Sensitivity (%)	Specificity (%)	Hausdorff5
(Zhang et al., 2020)	BRATS 2018	87.20	—	—	5.62
(Aboelenein et al., 2020)	BRATS 2018	86.50	88.3	99.9	7.53
(Qin et al., 2022)	BRATS 2018	88.77	91.51	—	—
(Micallef et al., 2021)	BRATS 2019	87.09	86.71	99.41	8.21
Proposed Edge U-Net	(Cheng et al., 2015)	Men.: 88.8 Gli.: 91.76 Pit.: 87.28	Men.: 94.02 Gli.: 93.59 Pit.: 85.99	Men.: 99.45 Gli.: 99.5 Pit.: 99.71	—

highly accurate tumor tissue segmentation was generated. We can conclude that CLAHE helped enhance contrast in MRIs by contrasting the Edge U-Net feature maps, labelled g, h, and i in Fig. 15, with the feature maps of the U-Net model, labelled d, e, and f in Fig. 15. The other models used only the median and Gaussian filters. The application of these filters resulted in feature maps with less noisy pixels.

Fig. 16 compares the parameter numbers of these segmentation models. The FCN8 model had the most model parameters, followed by the Res-UNet model, which had the fewest.

4.3.2. Comparison with other models on different datasets

In order to assess the robustness of brain tumor segmentation, the performance of the proposed model (Edge U-Net) was compared to that of general state-of-the-art models. Some brain tumor datasets classify brain tumors into low-grade gliomas (LGG) or high-grade gliomas (HGG). To compare our model to other state-of-the art models, we needed to reclassify meningiomas and pituitary tumors collectively as LGGs and gliomas as HGGs (Buchy et al., 2019; Gesperger et al., 2020; Streckert et al., 2019). Table 6 shows the values of Dice, Jac coefficients, and sensitivity of five recent models compared to our model.

It is possible to discover more about the Edge U-Net method's usability from other deep learning segmentation research, including (Huang & Wan, 2022; Kermi et al., 2018; Russo, Liu, & Di Ieva, 2022; Shehab, Fahmy, Gasser, & El-Mahallawy, 2021). For automated MRI brain tumour segmentation, the investigations of (Kermi et al., 2018) employed DCNNs inspired by a U-Net model, together with Weighted Cross Entropy (WCE) and Generalized Dice Loss (GDL). While (Shehab et al., 2021) outlines a technique for brain tumour segmentation that is automated and relies on Deep Residual Learning Network (ResNet) to

get over deep neural network gradient problem. Also, the study of (Russo et al., 2022) investigates a model uses a spherical coordinate system, in that study, only the Dice metric is introduced. Moreover, (Huang & Wan, 2022) built a new residual learning model based on the architecture of U-Net, enriching the skip connections in order to improve the feature extraction effect. Another study proposed a new model utilising multiscale fuzzy C-means (MsFCM) to segment brain tumor tissues (Soleymanifard & Hamghalam, 2022), but it is clear that our suggested Edge U-Net segmentation model outperformed their methods.

Moreover, some studies such as (Aboelenein, Songhao, Koubaa, Noor, & Afifi, 2020; Micallef, Seychell, & Bajada, 2021; Qin et al., 2022; Zhang, Jiang, Dong, Hou, & Liu, 2020) provide brain tumor segmentation models. Their structure is based on the U-Net model, and datasets were reported without tumor type classification. To make a reliable comparison, we compared the results of these studies to our work. Our Edge U-Net model was found to have outperformed other state-of-the-art segmentation models in terms of Dice and sensitivity, as shown in Table 7.

4.4. Ablation studies

4.4.1. Impact of using EGB

To assess the effect of employing an EGB on the segmentation process, we introduced samples of random feature maps of the images into the EGB module (see Fig. 17(b)). The proposed Edge U-Net model takes advantage of MRI-boundary features maps, fusing them with MRI feature maps through an EGB module. The EGB module is used to generate feature maps with highlighted boundaries. The proposed Edge U-Net model's feature maps, when combined with the EGB module, can

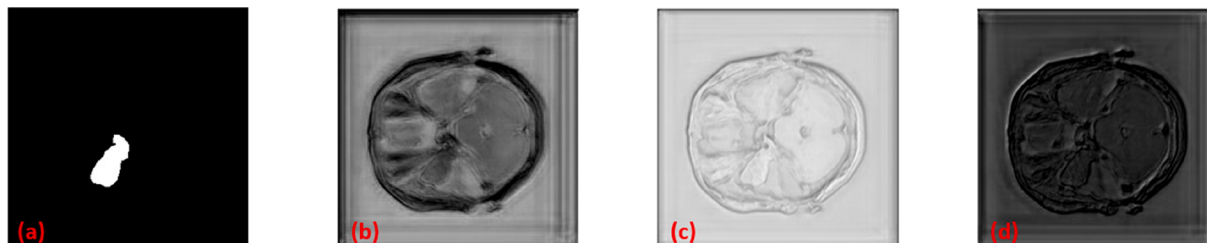


Fig. 17. Randomly selected feature maps for (a) Predicted mask, and (b, c, and d) present MRI feature map samples.

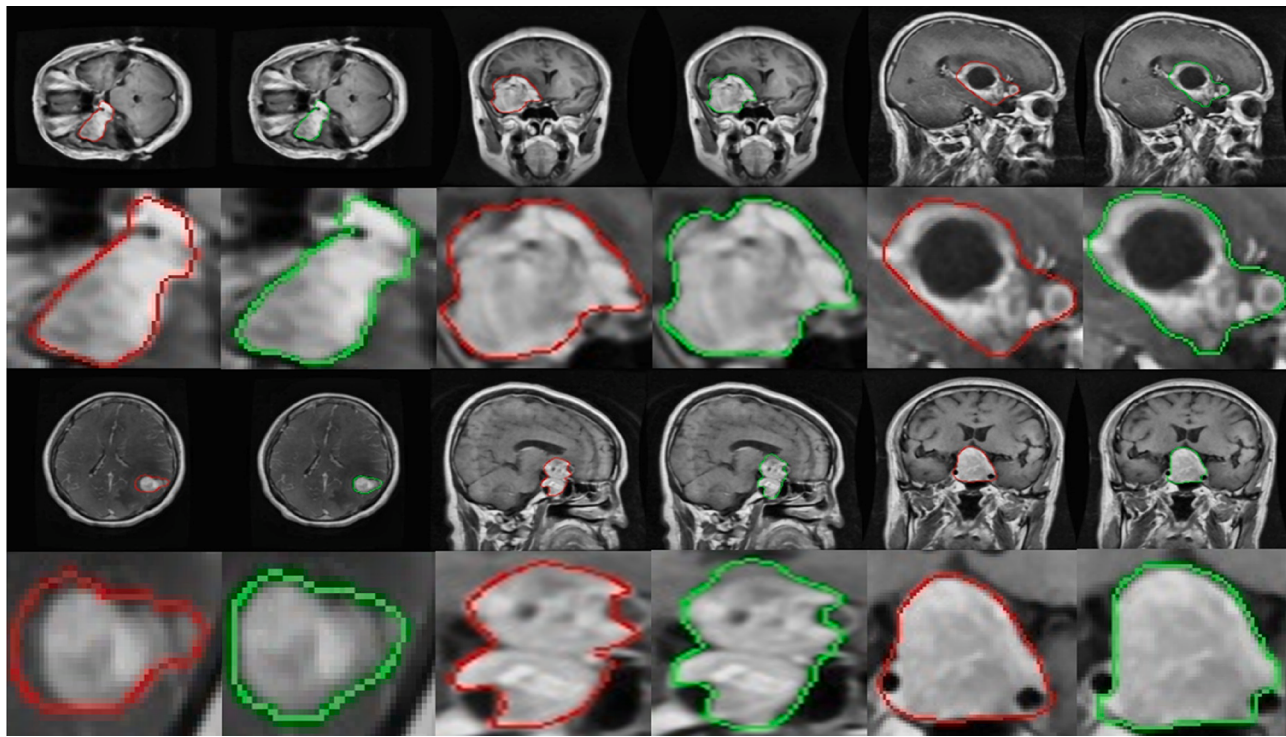


Fig. 18. Samples of brain tumor MRI segmentation (red: ground truth mask, green: proposed mask).

Table 8

Performance of the proposed framework using different loss functions.

Metric (%)	Meningioma			Glioma			Pituitary		
	Bin. loss	Bin. + Dice loss	Bin. + boundary Loss	Bin. loss	Bin. + Dice loss	Bin. + boundary Loss	Bin. loss	Bin. + Dice loss	Bin. + boundary Loss
Dice	88.03	87.04	88.8	89.08	89.49	91.76	87.14	85.76	87.28
Jac	78.62	77.07	79.85	80.31	80.99	84.78	77.22	75.01	77.43
Sensitivity	88.93	88.45	94.02	89.38	89.99	93.59	82.56	86.07	85.99
Specificity	99.71	99.68	99.45	99.44	99.45	99.5	99.8	99.62	99.71
Accuracy	99.47	99.43	99.51	98.97	99.01	99.23	99.31	99.29	99.35
Precision	88.92	88.44	89.4	89.38	89.99	93.59	82.56	86.07	85.99
AUC	93.45	92.72	94.85	94.12	94.26	94.85	95.88	92.54	94.12
MCC	87.76	86.77	85.99	88.54	88.98	91.38	86.94	85.39	86.96
Kappa	87.76	86.76	88.5	88.53	88.97	91.36	86.79	85.39	91.36
AHD	8.54	8.54	8.0	8.25	8.06	7.62	8.06	8.06	7.07

help accurately detect the boundaries of tumor tissue, allowing the model to track the tumor edge (see Fig. 17(a)), resulting in accurate segmentation of tumor tissues.

4.4.2. Visual comparisons by an experienced radiologist

Images from the test group with different axis (axial, sagittal, and coronal) were chosen, and the radiologist was asked to confirm that generated masks were accurate. Fig. 18 depicts a visual comparison of our method with masks from the dataset. When compared to the dataset masks, the proposed model produced more highly accurate segmentation. When drawing the boundaries of tumor tissues, the results were especially good. Our method was especially accurate when creating masks for tumors with irregular, complex, and fuzzy edges.

4.4.3. Comparison of using different loss functions

We trained our proposed Edge U-Net model against a variety of loss functions, including binary cross-entropy loss, dice loss, and a combination of binary cross-entropy and boundary loss. Performance of the proposed model, with the use of the aforementioned loss functions is detailed in Table 8. When we used the binary-cross entropy loss function alone, the model focused on just the pixel-wise classification. The best

performance was achieved when using an amalgamation of the binary cross-entropy and boundary loss with maximum Dice of 88.8 %, 91.76 %, and 87.28 % for meningiomas, gliomas, and pituitary tumors, respectively. The Jac for meningiomas stood at 79.85 %, for gliomas at 84.78 % and for pituitary tumor at 77.43 %. These results strongly indicated that binary cross-entropy and boundary loss need to be used concomitantly for the most efficacious brain tumor segmentation. Other performance metrics are present in Table 8.

5. Conclusions

Brain tumors, unlike normal brain tissue, can appear in different locations within the brain and have unpredictable shapes, structures, sizes, and boundaries. As a result, the most sensitive and specific segmentation method is required. In this study, a CLAHE was used to improve MRI quality and an Edge U-Net learning model-based framework that incorporated MRI boundaries was tested for its ability to more accurately segment the three types of brain tumor MRIs considered in this study. Image boundary features were used by EGB modules to feed the Edge U-Net model's decoder with rich semantic information from MRI boundaries, fusing them with image features to overcome information

loss during the predicted mask reconstruction. Furthermore, a novel loss function enabled the optimisation of tumor tissue boundaries, resulting in a highly accurate segmentation model. In terms of brain tumor tissue segmentation, experimental results showed that the proposed Edge U-Net model outperformed other models. Our model produced significantly higher and more accurate segmentation results compared to the other models, with the highest Dice of 88.8 %, 91.76 %, and 87.28 % for meningiomas, gliomas, and pituitary brain tumors respectively.

The advantages of our proposed framework appear to be the following: (1) significantly more accurate segmentation of tumors with complex edges; (2) well segmented radiology of brain tumors, including location, and shape; (3) the suggested model's generalisability was assessed on several types of brain tumors, confirming that it had outperformed state-of-the-art models. According to this study, the Edge U-Net model should be applied to a variety of brain tumors in the future. In order to improve the CAD systems, we may next evaluate the model's performance using tumor MRIs of various sizes and from other datasets. Finally, other edge-related algorithms can be employed to improve segmentation performance.

Funding

This research received no external funding.

CRediT authorship contribution statement

Ahmed M. Gab Allah: Conceptualization, Methodology, Data curation, Software, Writing – review & editing. **Amany M. Sarhan:** Conceptualization, Resources, Visualization, Writing – review & editing. **Nada M. Elshennawy:** Conceptualization, Validation, Writing – original draft.

Declaration of Competing Interest

The authors declare that they have no known competing financial interests or personal relationships that could have appeared to influence the work reported in this paper.

Data availability

No data was used for the research described in the article.

References

- Abdel-Maksoud, E., Elmogy, M., & Al-Awadi, R. (2015). Brain tumor segmentation based on a hybrid clustering technique. *Egyptian Informatics Journal*, 16(1), 71–81.
- Abuelenein, N. M., Songhao, P., Koubaa, A., Noor, A., & Afifi, A. (2020). HTTU-Net: Hybrid Two Track U-Net for automatic brain tumor segmentation. *IEEE Access*, 8, 101406–101415.
- Al-Hadeethi, H., Abdulla, S., Diykh, M., & Green, J. H. (2021). Determinant of covariance matrix model coupled with adaboost classification algorithm for EEG seizure detection. *Diagnostics*, 12(1), 74.
- Almahfud, M. A., Setyawan, R., Sari, C. A., & Rachmawanto, E. H. (2018). In *An Effective MRI Brain Image Segmentation using Joint Clustering (K-Means and Fuzzy C-Means)* (pp. 11–16). IEEE.
- Alqazzaz, S., Sun, X., Yang, X., & Nokes, L. (2019). Automated brain tumor segmentation on multi-modal MR image using SegNet. *Computational Visual Media*, 5(2), 209–219. <https://doi.org/10.1007/s41095-019-0139-y>
- Anitha, V., & Murugavalli, S. (2016). Brain tumour classification using two-tier classifier with adaptive segmentation technique. *IET Computer Vision*, 10(1), 9–17.
- Arab, A., Chinda, B., Medvedev, G., Siu, W., Guo, H., Gu, T., ... Song, X. (2020). A fast and fully-automated deep-learning approach for accurate hemorrhage segmentation and volume quantification in non-contrast whole-head CT. *Scientific Reports*, 10(1), 1–12.
- Arabahmadi, M., Farahbakhsh, R., & Rezazadeh, J. (2022). Deep Learning for Smart Healthcare—A Survey on Brain Tumor Detection from Medical Imaging. *Sensors*, 22 (5), 1960.
- Ayachi, R., & Ben Amor, N. (2009). In *Brain tumor segmentation using support vector machines* (pp. 736–747). Springer.
- Badrinarayanan, V., Kendall, A., & SegNet, R. C. (2015). A deep convolutional encoder-decoder architecture for image segmentation. *ArXiv Preprint ArXiv:1511.00561*, 5.
- Bauer, S., Nolte, L.-P., & Reyes, M. (2011). In *Fully automatic segmentation of brain tumor images using support vector machine classification in combination with hierarchical conditional random field regularization* (pp. 354–361). Springer.
- Biratu, E. S., Schwenker, F., Ayano, Y. M., & Debelee, T. G. (2021). A survey of brain tumor segmentation and classification algorithms. *Journal of Imaging*, 7(9), 179.
- Blessy, S. A., & Sulochana, C. H. (2015). Performance analysis of unsupervised optimal fuzzy clustering algorithm for MRI brain tumor segmentation. *Technology and Health Care*, 23(1), 23–35.
- Buchy, M., Lapras, V., Rabilloud, M., Vasiljevic, A., Borson-Chazot, F., Jouanneau, E., & Raverot, G. (2019). Predicting early post-operative remission in pituitary adenomas: Evaluation of the modified knosp classification. *Pituitary*, 22(5), 467–475.
- Chen, L.-C., Zhu, Y., Papandreou, G., Schroff, F., & Adam, H. (2018). Encoder-decoder with atrous separable convolution for semantic image segmentation. In *Proceedings of the European Conference on Computer Vision (ECCV)* (pp. 801–818).
- Cheng, J., Huang, W., Cao, S., Yang, R., Yang, W., Yun, Z., ... Feng, Q. (2015). Enhanced performance of brain tumor classification via tumor region augmentation and partition. *PLoS One*, 10(10), Article e0140381.
- Debelee, T. G., Amirian, M., Ibenthal, A., Palm, G., & Schwenker, F. (2017). In *Classification of mammograms using convolutional neural network based feature extraction* (pp. 89–98). Springer.
- Debelee, T. G., Kebede, S. R., Schwenker, F., & Shewarega, Z. M. (2020). Deep learning in selected cancers' image analysis—a survey. *Journal of Imaging*, 6(11), 121.
- Deng, G., & Cahill, L. W. (1993). In *An adaptive Gaussian filter for noise reduction and edge detection* (pp. 1615–1619). IEEE.
- Díaz-Pernas, F. J., Martínez-Zarzuela, M., Antón-Rodríguez, M., & González-Ortega, D. (2021). A deep learning approach for brain tumor classification and segmentation using a multiscale convolutional neural network. *Healthcare*, 9(2), 153. Multidisciplinary Digital Publishing Institute.
- Ding, Y., Chen, F., Zhao, Y., Wu, Z., Zhang, C., & Wu, D. (2019). A stacked multi-connection simple reducing net for brain tumor segmentation. *IEEE Access*, 7, 104011–104024.
- El-Shafai, W., Mahmoud, A. A., El-Rabaie, E.-S.-M., Taha, T. E., Zahran, O. F., El-Fishawy, A. S., ... Abd El-Samie, F. E. (2022). Hybrid Segmentation Approach for Different Medical Image Modalities. *CMC-COMPUTERS MATERIALS & CONTINUUM*, 33(2), 3455–3472.
- Frid-Adar, M., Diamant, I., Klang, E., Amitai, M., Goldberger, J., & Greenspan, H. (2018). GAN-based synthetic medical image augmentation for increased CNN performance in liver lesion classification. *Neurocomputing*, 321, 321–331. <https://doi.org/10.1016/j.neucom.2018.09.013>
- Gab Allah, A. M., Sarhan, A. M., & Elshennawy, N. M. (2021). Classification of Brain MRI Tumor Images Based on Deep Learning PGGAN Augmentation. *Diagnostics*, 11(12), 2343.
- Gesperger, J., Lichtenegger, A., Roetzer, T., Salas, M., Eugui, P., Harper, D. J., ... Mercea, P. A. (2020). Improved diagnostic imaging of brain tumors by multimodal microscopy and deep learning. *Cancers*, 12(7), 1806.
- Goodfellow, I., Bengio, Y., & Courville, A. (2016). *Deep learning*. MIT press.
- Gupta, G. (2011). Algorithm for image processing using improved median filter and comparison of mean, median and improved median filter. *International Journal of Soft Computing and Engineering (IJSCE)*, 1(5), 304–311.
- Haj-Hosseini, N., Milos, P., Hildesjö, C., Hallbeck, M., Richter, J., & Wårdell, K. (2016). Fluorescence spectroscopy and optical coherence tomography for brain tumor detection. *SPIE Photonics Europe, Biophotonics: Photonic Solutions for Better Health Care*. Brussels, Belgium: SPIE-International Society for Optical Engineering.
- Havaei, M., Davy, A., Warde-Farley, D., Biard, A., Courville, A., Bengio, Y., ... Larochelle, H. (2017). Brain tumor segmentation with deep neural networks. *Medical Image Analysis*, 35, 18–31.
- Hesamian, M. H., Jia, W., He, X., & Kennedy, P. (2019). Deep learning techniques for medical image segmentation: Achievements and challenges. *Journal of Digital Imaging*, 32(4), 582–596.
- Huang, C., & Wan, M. (2022). Automated segmentation of brain tumor based on improved U-Net with residual units. *Multimedia Tools and Applications*, 81(9), 12543–12566.
- Irwin, F. G. (1968). An isotropic 3x3 image gradient operator. *Presentation at Stanford AI Project*, 2014(02).
- İşın, A., Direkoglu, C., & Şah, M. (2016). Review of MRI-based brain tumor image segmentation using deep learning methods. *Procedia Computer Science*, 102, 317–324.
- Jadon, S. (2020). In *A survey of loss functions for semantic segmentation* (pp. 1–7). IEEE.
- Kaur, N., & Sharma, M. (2017). In *Brain tumor detection using self-adaptive K-means clustering* (pp. 1861–1865). IEEE.
- Kaya, I. E., Pehlivanlı, A.Ç., Sekizkardeş, E. G., & İbrkiç, T. (2017). PCA based clustering for brain tumor segmentation of T1w MRI images. *Computer Methods and Programs in Biomedicine*, 140, 19–28.
- Kebede, S. R., Debelee, T. G., Schwenker, F., & Yohannes, D. (2020). Classifier based breast cancer segmentation. *Journal of Biomimetics, Biomaterials and Biomedical Engineering*, 47, 41–61. Trans Tech Publ.
- Kermi, A., Mahmoudi, I., & Khadir, M. T. (2018). Deep convolutional neural networks using U-Net for automatic brain tumor segmentation in multimodal MRI volumes. *International MICCAI Brainlesion Workshop*, 37–48. Springer.
- Kim, Y.-T. (1997). Contrast enhancement using brightness preserving bi-histogram equalization. *IEEE Transactions on Consumer Electronics*, 43(1), 1–8.
- Krishnakumar, S., & Manivannan, K. (2021). Effective segmentation and classification of brain tumor using rough K means algorithm and multi kernel SVM in MR images. *Journal of Ambient Intelligence and Humanized Computing*, 12(6), 6751–6760.

- Li, H., Li, A., & Wang, M. (2019). A novel end-to-end brain tumor segmentation method using improved fully convolutional networks. *Computers in Biology and Medicine*, 108, 150–160.
- Long, J., Shelhamer, E., & Darrell, T. (2015). Fully convolutional networks for semantic segmentation. In *Proceedings of the IEEE Conference on Computer Vision and Pattern Recognition* (pp. 3431–3440).
- Luo, Z., Mishra, A., Achkar, A., Eichel, J., Li, S., & Jodoin, P.-M. (2017). Non-local deep features for salient object detection. In *Proceedings of the IEEE Conference on Computer Vision and Pattern Recognition* (pp. 6609–6617).
- Ma, C., Luo, G., & Wang, K. (2018). Concatenated and connected random forests with multiscale patch driven active contour model for automated brain tumor segmentation of MR images. *IEEE Transactions on Medical Imaging*, 37(8), 1943–1954.
- Magadza, T., & Viriri, S. (2021). Deep learning for brain tumor segmentation: A survey of state-of-the-art. *Journal of Imaging*, 7(2), 19.
- Maji, D., Sigedar, P., & Singh, M. (2022). Attention Res-UNet with Guided Decoder for semantic segmentation of brain tumors. *Biomedical Signal Processing and Control*, 71, Article 103077.
- Megersa, Y., & Alemu, G. (2015). Brain tumor detection and segmentation using hybrid intelligent algorithms. *AFRICON 2015*, 1–8. IEEE.
- Menze, B. H., Jakab, A., Bauer, S., Kalpathy-Cramer, J., Farahani, K., Kirby, J., ... Wiest, R. (2014). The multimodal brain tumor image segmentation benchmark (BRATS). *IEEE Transactions on Medical Imaging*, 34(10), 1993–2024.
- Micallef, N., Seychell, D., & Bajada, C. J. (2021). Exploring the U-Net++ Model for Automatic Brain Tumor Segmentation. *IEEE Access*, 9, 125523–125539.
- Milletari, F., Navab, N., & Ahmadi, S.-A. (2016). In *V-net: Fully convolutional neural networks for volumetric medical image segmentation* (pp. 565–571). IEEE.
- Müller, D., Hartmann, D., Meyer, P., Auer, F., Soto-Rey, I., & Kramer, F. (2022). MISEval: A Metric Library for Medical Image Segmentation Evaluation. *ArXiv Preprint*. ArXiv: 2201.09395.
- Mumford, D. B., & Shah, J. (1989). Optimal approximations by piecewise smooth functions and associated variational problems. *Communications on Pure and Applied Mathematics*.
- Nyil, L. G., Udupa, J. K., & Zhang, X. (2000). New variants of a method of MRI scale standardization. *IEEE Transactions on Medical Imaging*, 19(2), 143–150.
- Pereira, S., Pinto, A., Alves, V., & Silva, C. A. (2016). Brain tumor segmentation using convolutional neural networks in MRI images. *IEEE Transactions on Medical Imaging*, 35(5), 1240–1251.
- Prima, S., Ayache, N., Barrick, T., & Roberts, N. (2001). In *Maximum likelihood estimation of the bias field in MR brain images: Investigating different modelings of the imaging process* (pp. 811–819). Springer.
- Qin, C., Wu, Y., Liao, W., Zeng, J., Liang, S., & Zhang, X. (2022). Improved U-Net3+ with stage residual for brain tumor segmentation. *BMC Medical Imaging*, 22(1), 1–15.
- Ricci, P. E., & Dungan, D. H. (2001). Imaging of low-and intermediate-grade gliomas. *Seminars in Radiation Oncology*, 11(2), 103–112. Elsevier.
- Ronneberger, O., Fischer, P., & Brox, T. (2015). In *U-net: Convolutional networks for biomedical image segmentation* (pp. 234–241). Springer.
- Russo, C., Liu, S., & Di Ieva, A. (2022). Spherical coordinates transformation pre-processing in Deep Convolution Neural Networks for brain tumor segmentation in MRI. *Medical & Biological Engineering & Computing*, 60(1), 121–134.
- Sajid, S., Hussain, S., & Sarwar, A. (2019). Brain tumor detection and segmentation in MR images using deep learning. *Arabian Journal for Science and Engineering*, 44(11), 9249–9261.
- Sheela, C. J. J., & Suganthi, G. (2019). Automatic brain tumor segmentation from MRI using greedy snake model and fuzzy C-means optimization. *Journal of King Saud University-Computer and Information Sciences*.
- Shehab, L. H., Fahmy, O. M., Gasser, S. M., & El-Mahallawy, M. S. (2021). An efficient brain tumor image segmentation based on deep residual networks (ResNets). *Journal of King Saud University-Engineering Sciences*, 33(6), 404–412.
- Simonyan, K., & Zisserman, A. (2014). Very deep convolutional networks for large-scale image recognition. *ArXiv Preprint*. ArXiv:1409.1556.
- Sobhaninia, Z., Rezaei, S., Karimi, N., Emami, A., & Samavi, S. (2020). In *Brain tumor segmentation by cascaded deep neural networks using multiple image scales* (pp. 1–4). IEEE.
- Soleymaniard, M., & Hamghalam, M. (2022). Multi-stage glioma segmentation for tumour grade classification based on multiscale fuzzy C-means. *Multimedia Tools and Applications*, 81(6), 8451–8470.
- Streckert, E. M. S., Hess, K., Sporns, P. B., Adeli, A., Brokinkel, C., Kriz, J., ... Spille, D. C. (2019). Clinical, radiological, and histopathological predictors for long-term prognosis after surgery for atypical meningiomas. *Acta Neurochirurgica*, 161(8), 1647–1656.
- Sun, L., Ma, W., Ding, X., Huang, Y., Liang, D., & Paisley, J. (2019). A 3D spatially weighted network for segmentation of brain tissue from MRI. *IEEE Transactions on Medical Imaging*, 39(4), 898–909.
- Thaha, M. M., Kumar, K., Murugan, B. S., Dhanasekeran, S., Vijayakarthick, P., Selvi, A. S., ... Roy, S. (2019). Brain tumor segmentation using convolutional neural networks in MRI images. *Journal of Medical Systems*, 43(9), 1–10. <https://doi.org/10.1007/978-3-319-24574-4>
- Tu, Z., Ma, Y., Li, C., Tang, J., & Luo, B. (2020). Edge-guided non-local fully convolutional network for salient object detection. *IEEE Transactions on Circuits and Systems for Video Technology*, 31(2), 582–593.
- Tustison, N. J., Avants, B. B., Cook, P. A., Zheng, Y., Egan, A., Yushkevich, P. A., & Gee, J. C. (2010). N4ITK: Improved N3 bias correction. *IEEE Transactions on Medical Imaging*, 29(6), 1310–1320.
- Wang, P., & Chung, A. C. S. (2022). Relax and focus on brain tumor segmentation. *Medical Image Analysis*, 75, Article 102259. <https://doi.org/10.1016/j.media.2021.102259>
- Wang, X., Yu, K., Dong, C., & Loy, C. C. (2018). Recovering realistic texture in image super-resolution by deep spatial feature transform. In *Proceedings of the IEEE Conference on Computer Vision and Pattern Recognition* (pp. 606–615).
- Wulandari, A., Sigit, R., & Bachtiar, M. M. (2018). Brain tumor segmentation to calculate percentage tumor using MRI. *2018 International Electronics Symposium on Knowledge Creation and Intelligent Computing (IES-KCIC)*, 292–296. IEEE.
- Yu, X., Zhou, Q., Wang, S., & Zhang, Y. (2022). A systematic survey of deep learning in breast cancer. *International Journal of Intelligent Systems*, 37(1), 152–216.
- Zhang, J., Jiang, Z., Dong, J., Hou, Y., & Liu, B. (2020). Attention gate resU-Net for automatic MRI brain tumor segmentation. *IEEE Access*, 8, 58533–58545.
- Zhang, Z., Liu, Q., & Wang, Y. (2018). Road extraction by deep residual u-net. *IEEE Geoscience and Remote Sensing Letters*, 15(5), 749–753.
- Zuiderveld, K. (1994). Contrast limited adaptive histogram equalization. *Graphics Gems*, 474–485.